University of Alberta

Excitation of Internal Waves in a Three-Layer Fluid

by

Adarsh P. Mehta

A thesis submitted to the Faculty of Graduate Studies and Research in partial fulfillment of the requirements for the degree of Master of Science

in

Applied Mathematics

Department of Mathematical Sciences

Edmonton, Alberta

Fall, 1999

National Library of Canada
Acquisitions and Bibliographic Services
395 Wellington Street
Ottawa ON K1A 0N4
Canada

Bibliothèque nationale du Canada
Acquisitions et services bibliographiques
395, rue Wellington
Ottawa ON K1A 0N4
Canada

Your file Votre référence

Our file Notre référence

The author has granted a non-exclusive licence allowing the National Library of Canada to reproduce, loan, distribute or sell copies of this thesis in microform, paper or electronic formats.

L'auteur a accordé une licence non exclusive permettant à la Bibliothèque nationale du Canada de reproduire, prêter, distribuer ou vendre des copies de cette thèse sous la forme de microfiche/film, de reproduction sur papier ou sur format électronique.

The author retains ownership of the copyright in this thesis. Neither the thesis nor substantial extracts from it may be printed or otherwise reproduced without the author's permission.

L'auteur conserve la propriété du droit d'auteur qui protège cette thèse. Ni la thèse ni des extraits substantiels de celle-ci ne doivent être imprimés ou autrement reproduits sans son autorisation.

0-612-47068-7

Canada

University of Alberta

Library Release Form

Name of Author: Adarsh P. Mehta

Title of Thesis: Excitation of Internal Waves in a Three-Layer Fluid

Degree: Master of Science

Year this Degree Granted: 1999

Permission is hereby granted to the University of Alberta Library to reproduce single copies of this thesis and to lend or sell such copies for private, scholarly, or scientific research purposes only.

The author reserves all other publication and other rights in association with the copyright in the thesis, and except as hereinbefore provided, neither the thesis nor any substantial portion thereof may be printed or otherwise reproduced in any material form whatever without the author's prior written permission.

Adarsh Mehta

18 Devere Drive,
Guelph, Ontario
N1G 2S9

Date: August 27, 1999

University of Alberta

Faculty of Graduate Studies and Research

The undersigned certify that they have read, and recommend to the Faculty of Graduate Studies and Research for acceptance, a thesis entitled **Excitation of Internal Waves in a Three-Layer Fluid** submitted by Adarsh P. Mehta in partial fulfillment of the requirements for the degree of Master of Science in Applied Mathematics.

Dr. B. R. Sutherland

Dr. T. B. Moodie

Dr. A. B. G. Bush

Date: August 18, 1999

પૂજ્ય માતાપિતા તથા બા

આપનાં અહર્નિશ
અમીસિંચન અને ઈશ્વરકૃપાથી
આ ધ્યેયસાધનની
પ્રેરણા અને શક્તિ મળી છે

સપ્રેમ, આદર્શ

Abstract

The Morning Glory, a naturally occuring atmospheric disturbance viewed over Northern Australia, is believed to be a manifestation of large-amplitude solitary waves. Through mathematical analysis aided by laboratory experiments, we hope to better understand the origin and evolution of this phenomenon. We perform a series of lock-release experiments in which we examine the flow within a three-layer, salt-stratified fluid. At a certain interface thickness in the stratified fluid, a gravity current excites a mode-2 solitary wave, appearing in the interfacial layer in front of the gravity current head, and the current stops propagating. Trailing the gravity current are large-amplitude trapped internal waves. We study the effect of interface thickness and density difference to determine the conditions under which the solitary wave occurs. We propose that this transition occurs because the gravity current resonantly couples with trapped internal waves for a sufficiently thick interface.

Acknowledgements

I would like to express my thanks to my supervisor, Dr. Bruce Sutherland, for providing me with guidance and advice in various areas of the research for this thesis. I would also like to thank him for his patience in helping me revise my thesis. In addition, his financial support during the summer was greatly appreciated. Thanks also to fellow graduate students, Paul Choboter, Patrick Montgomery and Mateusz Reszka who were always willing to discuss various aspects of this study with me.

I gratefully acknowledge the financial support provided by the University of Alberta, Department of Mathematical Sciences in the form of a Teaching Assistantship.

Finally, words cannot begin to express my appreciation for my parents, my grandmother and my dear sister, Parul, whose encouragement has always been the most valuable assets to me.

Contents

1 Introduction **1**

1.1 Fluid motion in density stratified fluids 1

1.2 Gravity currents in stratified fluids 8

1.3 Solitary waves in stratified fluids 11

1.4 Generation of solitary waves by a gravity current 19

2 Theory **23**

2.1 The Three-Layer Model 23

2.2 Numerical solutions 33

2.3 Speed of the Intrusion 38

2.4 Speed of the Solitary Wave 46

2.5 Momentum Balance 52

3 Experimental Observations **57**

3.1 Experimental Procedures 57

3.2 Observations 66

3.3 Future Improvements on Data Collection 78

4 Conclusions **85**

Bibliography **89**

List of Tables

2.1 Key formulae in dimensional units. 56

3.1 Checklist of experiments performed. 66
3.2 Average amplitude in each run for two experiments. 67
3.3 Gravity current head speeds in four runs of an experiment. 70
3.4 Gravity current head speeds in the first run of several experiments. . 71
3.5 Speeds of the gravity current head and internal wave. 72
3.6 Horizontal distance from the lock at which the solitary wave appears. 74
3.7 Estimates of components of momentum for several experiments. . . . 75
3.8 Distance at which the solitary wave appears for different lock-lengths. 76

List of Figures

1.1 Atmospheric internal gravity waves made visible by clouds. 2
1.2 The leading Morning Glory roll cloud. 6
1.3 Schematic of the evolution of the flow in the experiments. 22

2.1 Schematic of internal waves in a three-layer fluid system. 24
2.2 Dispersion relations for internal waves in a three-layer fluid. 30
2.3 Phase speeds for internal waves in a three-layer fluid. 31
2.4 Phase speeds for the infinite- and finite-depth models. 32
2.5 Dispersion relations for the theoretical and numerical models. 36
2.6 Phase speeds for the theoretical and numerical models. 37
2.7 Schematic of an intrusive gravity current in a three-layer fluid. 38
2.8 Schematic of an internal bore in a two-layer fluid. 40
2.9 Bore speed and gravity current speed in a three-layer fluid. 45
2.10 Schematic of a solitary wave in a two-layer fluid. 46
2.11 Schematic of a double-humped solitary wave in a three-layer fluid. . . 47

3.1 Photographs of the intrusion at different times during an experiment. 60
3.2 Digitized images of the gravity current head and vertical time series. . 61
3.3 Horizontal time series for the fourth run of an experiment. 62
3.4 Schematic of the three-layer fluid experimental setup. 63
3.5 Schematic of a lock-release in three-layer fluid. 63
3.6 Density profiles for a two-layer fluid. 64

3.7 Density profile for a three-layer fluid. 65
3.8 Experimental and theoretical frequency for three different values of kh 79
3.9 Dispersion relation with corresponding experimental data. 80
3.10 Experimental gravity current speeds and internal wave phase speeds. 81
3.11 Experimental and theoretical gravity current speed and bore speed. . 82
3.12 Horizontal distance from the lock at which the solitary wave appears. 83
3.13 Experimental and theoretical solitary wave speeds. 84

4.1 Chain of effects. 87

Chapter 1

Introduction

1.1 Fluid motion in density stratified fluids

When density stratified fluids are disturbed, various fluid motions may arise due to gravitational forces and the variations in density. Some of the best known of these stratified-fluid motions are the gravity current, the internal gravity wave and the internal solitary wave.

Gravity waves are generated by the restoring force of gravity bringing a disturbed fluid system back to its undisturbed state (cf. Kundu, 1990, p. 185). When these waves occur at the surface of a liquid, they are called surface gravity waves. When they occur within a density stratified fluid, for example, at the interface between two fluids of different densities, they are called internal gravity waves. Buoyancy forces effectively reduce gravity so that the frequency, and hence the phase speed, of internal waves is smaller than that of surface waves (cf. Kundu, 1990, p. 227). Figure 1.1 shows an example of atmospheric internal gravity waves made visible by clouds. Under partly cloudy conditions, moisture lifted by the waves cools and consequently condenses at the peaks of the waves, thus rendering them visible as a clearly banded pattern.

Like the surface solitary wave, the internal solitary wave typically is a hump-

Figure 1.1: Internal gravity waves in the atmosphere made visible by clouds near Edson, Alberta. Photo taken by the author, June 12, 1998.

shaped disturbance of uniform velocity and virtually permanent form (cf. Simpson, 1997, p. 10). The surface solitary wave was first observed by Scott Russell in 1834 (Russell, 1844) when he noticed a mass of water in a channel accumulating around the prow of a boat, and then surging forward with great velocity, leaving the boat behind. On horseback, Russell followed this "large solitary progressive wave" of elevation, observing that it preserved its shape "some thirty feet long and a foot to a foot and a half in height" while propagating at nearly constant velocity for one or two miles before its height gradually attenuated. Russell investigated this phenomenon by constructing a series of laboratory experiments in which he created solitary waves by dropping a weight at one end of a water channel. By observing material particles suspended in the water, he was able to show that there was a net horizontal translation

of position which he took to be the volume of water to create the wave divided by the breadth of the channel. For a detailed history of the solitary wave, see Bullough (1987).

Solitary waves have been observed in the atmosphere to travel long distances without dispersion. A solitary wave maintains its shape due to a balance between linear dispersive effects, which tend to broaden the wavepacket, and weakly nonlinear effects, which act to steepen the wave. In a two-layer fluid, in which the upper and lower fluid are of different densities and depths, the internal solitary wave typically takes the shape of a single symmetrical hump of elevation or depression at the interface between the fluids rather than that of a periodic wave. If the lower layer is shallow, then the solitary wave is a hump of elevation. On the other hand, if the upper layer is shallow, then the solitary wave is a hump of depression. Keulegan's (1953) analysis excludes the formation of an internal solitary wave in a Boussinesq fuild when the two fluids are of equal depth. However, Amick & Turner (1986) derived a relation between the densities and layer depths which determines whether the solitary wave is a hump of elevation or depression. We let ρ_l and ρ_u denote the densities of the lower and upper layers respectively, and we let h_l and h_u denote the depths of the lower and upper layers respectively. Amick & Turner's (1986) result says that if

$$\rho_l(h_u)^2 > \rho_u(h_l)^2$$

then the solitary wave will be a hump of elevation, and if

$$\rho_l(h_u)^2 < \rho_u(h_l)^2$$

then the solitary wave will be a hump of depression. According to their theory, if the lower and upper layer depths are equal, then the solitary wave will be a hump of elevation.

Like the surface solitary wave investigated by Russell, the interfacial solitary wave displaces fluid a finite distance in the direction of propagation, with a net (horizontal) translation proportional to the characteristic length of the wave. This is different

from 'Stokes's drift' caused by nonlinear effects acting on large-amplitude waves. Stoke's drift is the gradual translation of particles in the direction of propagation of the periodic waves (cf. Kundu, 1990, p. 223). It is a second order effect resulting in particle orbits that do not form closed circular loops since a particle moves forward faster at the top of its trajectory and slower backward at the bottom of its trajectory. Consequently, for large-amplitude waves, there is a small net horizontal displacement which is uniform over the depth of the fluid for each period of the wave, a behaviour which is not observed in linear wave theory.

The gravity current, also known as a density current or buoyancy current, is a type of intrusion which occurs when a fluid of one density propagates through a quiescent fluid of another density, the driving force being gravity. (For example, an atmospheric gravity current can occur when there is mixing at an atmospheric inversion at the head of a cold front.) Gravity currents preserve nearly constant shape and speed before dissipating due to viscosity. Dissipation may also be a result of the Kelvin-Helmoltz mixing behind the gravity current head. The gravity current and internal gravity waves both transport momentum and energy, however there is also a clear transfer of mass with a gravity current, while small-amplitude internal gravity waves transport negligible mass. An excellent summary of observations and experiments of gravity currents is given by Simpson (1997).

The internal bore is another type of disturbance in a stratified fluid (*e.g.*, a two-layer fluid) which, like the gravity current, carries mass long distances. It is characterized by a sudden increase in the fluid depth (a jump) associated with a change in the flow rate (cf. Simpson, 1997, p. 5). Under certain conditions, a series of waves may appear close to the leading edge of the jump (Rottman & Simpson, 1989), in which case the intrusion is called an 'undular' bore. If the depth of the undisturbed fluid is close to zero, the bore closely resembles a gravity current. Unlike the gravity current, the bore is not necessarily generated by gravity acting as a restoring force. (For example, Rottman & Simpson generated internal bores in the laboratory by

towing an obstacle along the bottom of a tank containing a two-layer fluid.)

Manifestations of atmospheric gravity currents are found in geophysical phenomena such as cold fronts moving into warmer air (cf. Simpson, 1997, p. 49) and sea-breeze fronts which have a great impact on the transport of dust, airborne pollution and the spreading of insect pests (Simpson *et al.*, 1977). Gravity currents also appear as a consequence of thunderstorms (cf. Simpson, 1997, p. 12). In the tropics, warm moist air rises due to exceptionally strong convection until it reaches the tropopause. (At about 10 km above the surface of the earth is the tropopause, a 'boundary' between the lower atmosphere called the troposphere and the upper more stable layer called the stratosphere (cf. Pedlosky, 1979, p. 353). The weather is considered to take place below this boundary since there is little water vapour in the stratosphere due to its stability to vertical transport.) At the tropopause the moist air spreads out as an 'anvil' cloud. A severe type of thunderstorm outflow is the microburst, a very sudden downburst of cold air from a thunderstorm, having a strong wind-shear and downcurrent (Linden & Simpson, 1985). As the microburst decends, carried down by rain (*i.e.*, the cooling by the re-evaporation of rain), its density increases as the water drops evaporate, leaving behind cooled air. At ground level, it forms a strong dense gravity current propagating radially outward. If the outflow travels over dusty areas, a dramatic visualization occurs by the severe wind squalls at the gravity current front which raise dust from the ground. However, an outflow not made visible by dust or clouds can present a serious hazard to low- and high-flying aircraft. Often, the cold fronts and thunderstorm outflows are made visible by a thin 'rope cloud' at the leading edge of the front (cf. Simpson, 1997, p. 49). These rope clouds are created by the evaporation of rain from the edge of the front and, by tracking their progress through satellite images, can be used to explain the cause of meteorological conditions in its vicinity, information which is also useful for aircraft safety.

Although the difference between various types of internal disturbances may be clear in theory or in the laboratory, there is often ambiguity in the interpretation of

Figure 1.2: The leading Morning Glory roll cloud approaching Burketown, Australia from the north-east. Photo used with permission of Russell White, http://www.dropbears.com/brough/images.

atmospheric disturbances, even when they are made visible by clouds. Clarke (1998, fig. 1) describes an excellent example of an internal atmospheric disturbance in which a GOES-8 satellite image shows a periodic band of clouds generated south of a cold front in South Coastal Texas, April 14, 1997. However, it is not clear whether this is a result of internal waves, an undular bore, or a train of solitary waves. One of the most spectacular dramatizations of an atmospheric disturbance is the Morning Glory roll cloud observed in Northern Australia typically each year in late October (see figure 1.2). It provides another example of a disturbance which has its classification still open to interpretation. This phenomenon is characterized as a wind squall,

usually accompanied by a long, low-lying horizontal roll cloud or series of roll clouds occurring in the early morning, often originating over the Gulf of Carpentaria in North Australia (Clarke *et al.*, 1981). The leading roll cloud may have a height of around 2 km, a width of about 4 km and can be typically 100 to 1000 km in length, travelling for several hundred kilometers at a speed of anywhere from around 5 to 18 m/s.

Various theories have been proposed to determine the origin and evolution of the Morning Glory. Three types of morning glories have been observed around the Gulf of Carpentaria, each type classified by the direction from which the phenomenon propagates. Clarke (1972) suggested that the northeasterly to easterly morning glories could be produced by a propagating internal hydraulic jump resulting from the interaction of a katabatic (downslope) flow, generated on Cape York Peninsula (enclosing the Gulf on the east) with a discontinuous ground slope. In general, katabatic flow results from nocturnal downslope winds produced by hills and valleys and is characterized as a sharp cold gravity current front moving down a valley floor (cf. Simpson, 1997, p. 62). This theory for northeasterly to easterly morning glories was later revised by Clarke *et al.* (1981) who identified the Morning Glory as an internal undular bore caused by either a sea-breeze front interacting with a nocturnal inversion or, on occassion, by the effect of a katabatic flow. A suggested origin for southerly to southwesterly and southeasterly morning glories is the interaction of an advancing inland frontal heat trough with a nocturnal inversion (Christie *et al.*, 1981; Smith *et al.*, 1982; Smith & Ridely, 1990). The heat trough may be a result of convective mixing due to the sun heating the sand over the desert. Another possible mechanism generating southerly to southwesterly morning glories could be katabatic flow from the highlands to the south of the Gulf (Clarke, 1983b; Smith *et al.*, 1986). Christie (1992) proposes that southeasterly morning glories could originate in the interaction of katabatic flow from the more pronounced highlands to the south and southeast of the Gulf with a developing nocturnal inversion.

The existence of internal solitary waves in the atmosphere was first suggested by Abdullah (1949), and later investigated in more depth by Abdullah (1955) and Christie *et al.* (1978). The Morning Glory roll clouds themselves are thought to be associated with internal solitary waves at the leading edge of an internal bore or a decelerating gravity current, proceeding from the evolution of a gravity current-produced disturbance of the nocturnal or maritime inversion layer, a view supported by Christie *et al.* (1978, 1979), Clarke *et al.* (1981), Smith *et al.* (1982), Noonan & Smith (1985) and Christie (1989, 1992). The cloud is created when a sufficient amount of moist ambient air near the leading edge of the solitary wave is lifted to condensation level.

Christie (1992) summarizes previous suggestions on the decay of the Morning Glory waves: the decay could be due to turbulent frictional damping, the erosion of the inversion layer as a result of continued daytime convection over land, or loss of energy into the upper atmosphere.

Understanding the genesis and evolution of internal solitary waves becomes especially important in aviation. If solitary waves in the atmosphere occur as clear-air disturbances (not made visible by clouds), they can present a serious hazard to low-flying aircraft. In the present study, to be described in further detail in the final section of this chapter, we investigate the genesis of a solitary wave excited by a gravity current in a special case of a stratified fluid.

1.2 Gravity currents in stratified fluids

A gravity current in a stratified fluid may be sufficiently light that it travels along the top of an ambient fluid or sufficiently dense that it travels along the bottom. If the current has a density intermediate to the lowest and highest densities of an ambient stratified fluid, it will form an intrusion, for example, along an atmospheric inversion. In all cases, the front of the intrusion forms a 'head', the profile of which depends

on various properties present in the fluid system such as density gradients, viscosity, and background velocity. In turn, the gravity current head provides the main source of mixing between the ambient fluid and the intruding fluid, occurring in the shear instabilities behind the gravity current head, a highly turbulent zone.

The behaviour of the gravity current is highly dependent on the stratification of the ambient fluid. In a two-layer fluid, in which a uniform layer overlies a uniform layer of more dense fluid, the intrusion of fluid of intermediate density propagates along the interface between the fluids in the form of a gravity current if the mass flux of the fluid is sufficiently large. In the past, intrusions in two-layer fluids have received considerable attention in both theoretical investigations and laboratory experiments. By evaluating the momentum balance within each layer, assuming no mixing between the layers, neglecting stress terms at the fluid interface, and approximating the pressure at the interface to be the mean of the upstream and downstream pressures, Yih & Guha (1955) investigated jumps in a two-layer fluid system and verified their results with experimental observations. Benjamin (1968) derived the propagation speed of gravity currents for energy-conserving flow and flow with energy loss in fluids of infinite and finite vertical extent, then compared the theoretical predictions with experimental data. Holyer & Huppert (1980) extended Benjamin's (1968) work to steady, energy-conserving theory for gravity currents of prescribed volume flux entering a two-layer fluid either along the bottom of the ambient fluid or along the interface between the two fluids. They assume that the fluid flow is steady and irrotational and that there is no mixing between the fluids of different densities. For a sufficiently thick gravity current 'tail', they showed that the current loses energy, forming a wave train behind the current in order to maintain a momentum balance. To investigate the stability of the steady solution, their model included the effects of surface tension. (In the present investigation, we study the stationary wave train behind the current in a three-layer fluid, as well as the ensuing disturbance in front of the current.)

Through a series of laboratory experiments, Maxworthy (1980) observed the collapse of a region of mixed fluid from behind a lock toward its equilibrium state in a stratified ambient fluid. Both the mixed and ambient fluids were essentially two-layer fluids that had been allowed to diffuse, however, the thickness D over which density varied in the mixed fluid was larger than the thickness d over which density varied in the ambient fluid. The effect of the ratio of these thicknesses, D/d, and the effect of the lock length L on the ensuing flow was investigated. Maxworthy observed that the collapsed mixed region, propagating as a gravity current along the interfacial layer of the ambient fluid, generated a sequence of amplitude-ordered solitary waves in front of the gravity current head. As D/d and L/d increased, the number of solitary waves generated in front of the mixed fluid intrusion increased. It was suggested that these laboratory experiments had much in common with the explanation of the Morning Glory phenomenon given by Clarke (1972).

Britter & Simpson (1981) experimentally studied the structure of the head of an intrusive gravity current between two fluids of different densities to find a dependence of the flow on the interface thickness and depth of intrusion, the density of which was the mean of the two densities in the ambient fluid. The interface thickness was varied by allowing the two layers to diffuse. As the ratio of the interface thickness to current depth was increased, the Kelvin-Helmholtz billows around the gravity current head reduced in magnitude, until at a ratio close to 1 mixing between the two fluids at the head ceased. No details were given of possible trapped internal waves trailing behind the gravity current head.

Wood & Simpson (1984) studied intrusive jumps in layered miscible fluids. By towing an obstacle along the bottom of their laboratory flume through the lower layer of a two-layer Boussinesq fluid, they created a bore at the interface of the two fluids. They compared the observed speed of propagation of the bore to their theoretical speed obtained by assuming energy conservation in the lower layer. They also found that for a bore height greater than twice the height of the lower ambient layer, the

undular jump in many cases behaved like the head of a gravity current

Rottman & Simpson (1989) described the formation of intrusive bores by gravity currents in a two-layer system, where the gravity current propagated along the floor of the tank. They classified the generation of three types of bores based on the ratio of the intrusion's height, h_b, to the lower layer thickness, h. For $1 < h_b/h < 2$ they observed an undular and laminar bore, for $2 < h_b/h < 4$ they observed turbulent mixing behind the first crest of the undular bore, and for $h_b/h > 4$ the observed intrusion resembled a gravity current head.

More recently, Klemp *et al.* (1997) showed that the intrusive bore propagation speed is more accurately determined by assuming that energy loss occurs within the upper layer of a two-layer fluid, unlike Wood & Simpson (1984) who assumed that energy loss occurs within the lower layer. (We elaborate further on this in the next chapter.) The theoretical speed derived by Klemp *et al.* more closely resembled the observed speeds from Wood & Simpson's (1984) experiments. They also found that for bore heights larger than approximately half the ambient fluid depth, their bore speed was close to the theoretical gravity current speed given by Benjamin (1968).

In the present study, we investigate the characteristics of the trapped internal waves behind an intrusive gravity current. These trailing small-amplitude waves have received little attention in previous literature, but have been observed in the experiments of the present study. As mentioned above, the fundamental difference between the present and past experiments lies in the setup of the ambient fluid. In the present experiments, we focus on a three-layer fluid to investigate the resonant coupling between the gravity current and the internal gravity waves trailing the current.

1.3 Solitary waves in stratified fluids

Before reviewing previous investigations of solitary waves in stratified fluids, we shall summarize the history, leading to the Korteweg-de Vries (KdV) equation, of the sur-

face solitary wave as given by Bullough (1987) and Drazin & Johnson (1989, pp. 8-12). Much of the theory of surface solitary waves was extended by later authors for internal solitary waves.

Based on laboratory experiments of surface solitary waves, Russell (1844) determined that the volume of water displaced by the wave is equal to the volume of water in the wave. He also deduced empirically that the speed c of the solitary wave is given by

$$c = \sqrt{g(h+a)}, \tag{1.1}$$

where g is the acceleration due to gravity, a is the amplitude of the wave and h is the undisturbed depth of the ambient fluid. Further analysis on solitary wave theory was later taken up by Boussinesq (1871) and Rayleigh (1876). By assuming that a solitary wave has a length much greater than the depth of the water (shallow-water theory), and using the equations of motion for an inviscid incompressible fluid, Boussinesq (1871) was able to confirm Russell's formula (1.1). Starting from Euler's equation for momentum conservation in an incompressible fluid of density ρ having pressure gradient ∇p,

$$\rho \frac{D\mathbf{u}}{Dt} = -\nabla p + \rho \mathbf{g},$$

where $\mathbf{u} = (u, v, w)$ and $\frac{D}{Dt} \equiv \frac{\partial}{\partial t} + \mathbf{u} \cdot \nabla$ denotes a material derivative, together with an approximated conservation of mass,

$$\nabla \cdot \mathbf{u} = \mathbf{0},$$

Boussinesq reached the partial differential equation for the free surface elevation $f(x,t)$ given by

$$f_{tt} = c_0^2 f_{xx} + c_0^2 \left(\frac{3}{2} \frac{f^2}{h} + \frac{h^2}{3} f_{xx} \right)_{xx}, \tag{1.2}$$

where $c_0 = \sqrt{gh}$ is the linear wave speed. By finding a solitary wave solution for this equation, Boussinesq and Rayleigh showed that the solitary wave profile $z = f(x,t)$

is given by

$$f(x,t) = a\ \mathrm{sech}^2\Big[\frac{(3\frac{a}{h+a})^{1/2}}{2}\cdot\frac{x-ct}{h}\Big]. \tag{1.3}$$

Korteweg & de Vries (1895) were able to write down a simpler equation than (1.2), which admitted (1.3) as a solution. Their famous 'KdV equation' in scaled form (in a frame translating at speed c_0),

$$u_t + 6uu_x + u_{xxx} = 0, \tag{1.4}$$

forms the basis of much of the solitary wave theory which followed. (1.4) was derived for small-amplitude long waves using the governing equations of irrotational two-dimensional motion of an incompressible inviscid fluid with a free surface and rigid bottom boundary. Korteweg & de Vries found the speed of the solitary wave to be

$$c \sim \sqrt{gh}\Big[1+\frac{a}{2h}\Big], \tag{1.5}$$

which corresponds to Russell's (1844) empirical formula (1.1) to $O(\frac{a}{h})$.

A number of theoretical results have been reported on internal solitary waves propagating through stratified fluids. One of the earlier studies is Keulegan's (1953) investigation (based on KdV theory) of the characteristics of internal solitary waves in a two-layer fluid. Keulegan showed that an internal solitary wave with a length larger than the total ambient fluid depth has a profile similar to that of the surface solitary wave from KdV theory, namely, a sech^2 profile. For a Boussinesq fluid (assuming the density difference between the two fluids to be small) Keulegan determined an expression for the wave velocity as a function of wave height, density difference between the two layers and layer thicknesses.

Long (1956) also considered solitary waves propagating along the interface between two immiscible fluids, bounded above and below by rigid boundaries. He included a higher order approximation (to fifth order in $\frac{a}{h}$) for the speed of propagation for the internal solitary wave. Benjamin (1966) extended Long's (1956) shallow-water study to include other types of stratification, with a fixed or free upper boundary. As

in KdV theory, Benjamin's underlying assumption in the study of internal solitary waves was that the horizontal length scale of motion was long compared to the total fluid depth.

A new class of solitary waves, namely, internal solitary waves in infinitely deep fluid systems, were concurrently investigated by Benjamin (1967) and Davis & Acrivos (1967). The latter authors considered an internal solitary wave propagating through an ambient fluid of infinite-extent in which two layers of different densities were separated by a thin layer where the density varied continuously. Their analysis assumed that the wavelength of the disturbance was large compared to the thickness of the region in which the density was not constant. They wrote down the governing partial differential equations in terms of velocity potentials for each of the three layers (the upper and lower layers of constant density, and the middle layer of varying density), along with boundary conditions for velocity and pressure continuity between the layers. The long wave assumption allowed them to use a stretched horizontal co-ordinate $\hat{x} = \varepsilon x$ with $\varepsilon \ll 1$. A similarly stretched vertical co-ordinate prevented the equations in the lower and upper layers (of constant density) from degenerating completely. They performed a small parameter expansion on the main dependent variables of the system and completed their theoretical analysis by employing the method of inner and outer expansions. Finally, they arrived at an equation for the internal solitary wave profile,

$$f(x) = \frac{a\lambda}{(x - ct)^2 + \lambda^2}, \tag{1.6}$$

where c is the propagation velocity of the solitary wave. Unlike the sech^2 profile of the KdV (shallow-water) theory, this algebraic solitary wave (in deep water) shows a dependence on the characteristic half-width λ of the solitary wave. Davis & Acrivos also compared their theory to experiments in which they created solitary waves at the interface between two fluids which had been allowed to diffuse over time to create a region of varying density. As part of their experimental apparatus, they fitted an open-topped box with a plunger, and positioned the box in the fluid so that

the horizontal slit on one side of the box was aligned with (and facing) the density gradient layer. A solitary wave was created by drawing fluid into the box and ejecting it through the slit with the help of the plunger. Upon comparing their observations with their theory, they determined that neither the viscosity nor the finite depth of the fluid (40 cm) had a significant influence on the speed of propagation of the solitary wave. They also determined that the idealized density profile from their theory adequately represented the experimental configuration.

The profile given by (1.6) was independently derived by Benjamin (1967), whose main assumption in the analysis of deep-water solitary waves was that $a\lambda = O(h^2)$. Assuming a solution of the form $u = \hat{u}(z)e^{i(\omega t - kx)}$, in order to obtain the dispersion relation to leading terms for infinitesimal long waves in a deep fluid system,

$$\omega = kc_0(1 - \gamma|k|),$$

with $\gamma > 0$, Benjamin wrote down the equation

$$u_t + c_0 u_x = c_0 \gamma |k| u_x. \tag{1.7}$$

Next, he assumed that the wave vanished at $x = \pm\infty$ so that (1.7) could be generalized by the Fourier integral theorem to

$$u_t + c_0 u_x = c_0 \gamma \mathcal{F}(u_x), \tag{1.8}$$

where

$$\mathcal{F}(\xi(x)) = \frac{1}{2\pi} \int_{-\infty}^{\infty} |k| e^{-ikx} \left\{ \int_{-\infty}^{\infty} \xi(x') e^{ikx'} \, dx' \right\} dk.$$

Benjamin explained the physical meaning of $-\mathcal{F}(\xi(x))$ as "the hydrodynamic pressure on an infinitesimal hump described by $z = \xi(x)$, over which there is an irrotational flow of an infinite fluid with unit density and velocity". Finally, he modified (1.8) to include the effects of finite amplitude,

$$u_t + c_0 u_x + C u u_x = c_0 \gamma \mathcal{F}(u_x), \tag{1.9}$$

where C is a constant. (For a wave propagating toward a region at rest in which $u = 0$, Benjamin (1967) says that the dependent variable u is conserved along a characteristic given to a first approximation by $dx/dt = c_0 + Cu$.) This (*i.e.*, (1.9)) was Benjamin's (1967) counterpart to the KdV equation. Benjamin found the exact solution to (1.9) to be the solitary wave whose profile is given by (1.6).

In addition to the stratification used by Davis & Acrivos (1967), Benjamin (1967) extended his analysis to included other infinite-depth stratified fluid configurations. He also compared his theory to experiments. Internal solitary waves were generated in a two-layer fluid in which the upper fresh-water layer was a half inch deep and the lower salt-water layer was 6 inches deep. A wooden cylinder spanning the narrow fluid tank was placed in the upper layer, and a rigorous initial disturbance was created by pushing the cylinder a few inches toward the opposite end of the tank. Benjamin observed a solitary wave of depression propagating along the interface between the fluids. The ambient fluid in the experiments was sufficiently deep to be modelled by deep-water theory.

Hurdis & Pao (1975) found that their experimental observations of small-amplitude internal solitary waves in a stratified fluid were in close agreement to Benjamin's and Davis & Acrivos' theoretical predictions. Hurdis & Pao's 60 cm-deep two-layer fluid consisted of a layer of fresh water on top of a layer of salt water that had been allowed to diffuse, creating a thin transition region at the interface. An internal solitary wave was created by towing a vertical flat plate through the interface. The experiment was repeated for various towing speeds and for various density profiles.

Benjamin's (1967) theory was later generalized by Ono (1975). Using a nonlinear perturbation method, Ono extended Benjamin's steady wave theory to derive a time-dependent integro-differential equation (the Benjamin-Davis-Ono (BDO) equation) governing the unsteady behaviours of internal waves in stratified fluids of great depth. It was shown that the resultant equation admits an internal algebraic solitary wave as a particular steady solution, whose profile is given by (1.6).

At this point, it is useful to summarize the main differences between BDO theory and the KdV theory as extended by Keulegan (1953), Long (1956), and Benjamin (1966) for small-amplitude internal solitary waves. KdV theory (for internal waves) holds for long shallow-water solitary waves for which the wavelength λ of the disturbance is much greater than the total fluid depth H. For a solitary wave with amplitude a, $a\lambda^2 = O(H^3)$. For small enough values of k, the KdV equation yields a dispersion relation of the form $\omega = kc_0(1 - \beta k^2)$ with $\beta = \frac{1}{6}h^2$, and yields a sech^2 solitary wave profile given by (1.3). BDO theory holds for long deep-water internal solitary waves for which the wavelength of the disturbance is much smaller than the total fluid depth, but much greater than the depth d of the region over which the density varies continously. The governing relation for the various length scales involved is $a\lambda = O(d^2)$, where $d \ll H$. (For the KdV case, $d = O(H)$.) The BDO equation yields a dispersion relation of the form $\omega = kc_0(1 - \gamma|k|)$ with $\gamma > 0$, and yields an algebraic solitary wave profile given by (1.6).

Koop & Butler (1981) carried out an experimental investigation comparing observations to shallow-water (KdV) theory and deep-water (BDO) theory. They found that the range of validity of the KdV model was larger than could be expected theoretically. A single downward displacement of a paddle straddling the interface between two fluids generated an internal solitary wave propagating along this interface. However, they noted a discrepancy between theory and large-amplitude solitary waves.

These large-amplitude solitary waves were also investigated experimentally by Stamp & Jacka (1995). They generated a single large-amplitude internal solitary wave in a deep two-layer fluid by horizontally displacing a paddle along the diffused interface between the two layers of different densities. The observed disturbance was described as an "isolated large-amplitude mode-2 solitary wave (lowest-order varicose mode)" with a mode-1 wave (lowest-order sinuous mode) closely following. By varying the generation technique and reducing the depth d of the interface, Stamp & Jacka were able to obtain small-amplitude solitary waves. They compared observations of waves

of different amplitudes and found, as predicted, that BDO theory failed to predict the behaviour of large-amplitude waves, while small-amplitude waves ($\frac{a}{d} \leq \frac{1}{2}$) were well-described by the theory. In particular, the propagation speeds for the small-amplitude waves were predicted by theory, but for larger amplitudes the measurements were underestimated. In addition, at small amplitudes, they observed that λ decreased as a increased, as predicted by weakly non-linear theory, but at large amplitudes, λ increased as a increased. They also determined that small waves carried energy and momentum whereas sufficiently large waves also carried mass long distances.

Internal solitary waves in a two-layer fluid were also investigated experimentally by Michallet & Barthélemy (1998) using a two-immiscible-fluid system to prevent diffusion between the two layers. The ambient fluid consisted of a layer of petrol on top of a layer of water. Behind a gate, the fluid was similary set up, however, the interface level was modified so as to be deeper than interface level in the ambient fluid. When the gate was lifted, a group of solitary waves was observed. Comparison with previous solitary wave theory was considered inappropriate, since the density difference in their experiments was rather large ($\sim 22\%$).

Comparisons with internal solitary wave theory have not only been made for laboratory observations, but also for observations of solitary waves in the atmosphere and ocean. Following Koop & Butler (1981), Noonan & Smith (1985) found that the Morning Glory solitary wave is better described by BDO theory, rather than KdV theory. Ostrovsky & Stepanyants (1989) presented observations of internal solitary waves in shallow seas and deep ocean regions. They compared their data, collected over two decades, to theoretical predictions based on the KdV, BDO and Joseph (1977) solitary wave solutions. Generally, as expected, the BDO algebraic solitary wave profile best fit the profiles obtained from their collected data. However, solitary wave speeds were better predicted by KdV theory.

1.4 Generation of solitary waves by a gravity current

Not well understood are the dynamics of the transition from a flow consisting of a gravity current propagating along an inversion to a flow in which an internal solitary wave is spawned by the gravity current. In a particularly important experimental study lending an interpretation of non-linear internal waves in the atmosphere and ocean, Maxworthy (1980) investigated the behaviour of BDO type solitary waves excited by an intrusion in a two-layer fluid where the interface was left to diffuse. The experiments had much in common with the Morning Glory phenomenon, thus offering an explanation for the observed cloud pattern. Maxworthy remarked that "if a given physical system is capable of supporting solitary wave motions then such motions will invariably arise from quite general excitations". More laboratory situations of a gravity current exciting solitary waves were reported in experiments by Rottman & Simpson (1989), Noh *et al.* (1992) and Manasseh *et al.* (1998). Rottman & Simpson simulated a gravity current travelling along the floor of a tank in a two-layer fluid by towing an obstacle along the floor. They observed an undular bore developing at the interface in front of the obstacle. (Upon considering Maxworthy's comment above, this disturbance might be a group of solitary waves.) Noh *et al.* (1992) observed solitary waves generated by an intrusive fluid (a 'thermal') propagating along a density interface. They suggested that their experiments may model thunderstorm events. As an analogue of a thunderstorm microburst, the experimental fluid system studied by Manasseh *et al.* (1998) consisted of a constant-density upper layer over a linearly stratified lower layer. They created a thermal which propagated through the lower continuously stratified layer, and observed a solitary wave developing over the thermal, which in turn lost mass and stopped propagating at around $x = 20$ cm.

To understand better the origin and evolution of a phenomenon such as the Morning Glory, a simplified laboratory investigation focusing on ambient stratification, and neglecting background shear, compressibility and viscosity, was initiated by Maxworthy (1980). Intrusive flows in which a gravity current excites a solitary wave

in a two-layer fluid have already received some attention. However, with repeated intrusions causing mixing, a more realistic ambient fluid system would be continuously stratified over a region between the upper and lower fluids. (In the laboratory, two-layer miscible fluids are more realistically continuously stratified since diffusion occurs across the interface, but in past experiments the thickness of this interface has been small compared to the height of the disturbance.) As a step toward the continuously stratified system, it is useful to determine the various wave behaviours in a three-layer system. A system of this type is amenable to a simple analytic and experimental study. Furthermore, study of a three-layer system is promoted by density profiles of the Morning Glory's atmosphere just prior to the occurrence of the phenomenon, based on data collected and compiled by Menhofer *et al.* (1997, fig. 4). In fact, this type of three-layer profile was also determined in the Caspian Sea, followed by observations of internal solitary waves along a bore front (Ostrovsky & Stepanyants, 1989, fig. 1).

The present investigation deals with a three-layer fluid in which the lower and uppers layers are of equal depth, and the middle layer has a density which is the mean of the outer two layers. In a series of lock-release experiments, we examine the behaviour of the flow within a three-layer salt-stratified fluid. These reveal that at a certain thickness of the middle layer, an intrusive gravity current excites an internal 'double-humped' solitary wave in front of the gravity current head, and the current itself stops propagating. This double-humped solitary wave, initially developing over the gravity current head and gradually moving forward, may be viewed as two solitary waves, one of depression and one of elevation, propagating together in phase. Trailing the gravity current are large-amplitude trapped internal waves. We propose that this transition occurs because the gravity current resonantly couples with trapped internal waves for a sufficiently thick interface, the waves acting to extract momentum from the current. The evolution of the intrusion is depicted in the schematic given in figure 1.3.

In Chapter 2, we perform some mathematical analysis developed for a three-layer fluid to determine various properties, including a momentum balance, of the gravity current, the trapped internal waves and the solitary wave. Observations from experiments show that the observed flow is approximately two-dimensional, thus a span-wise uniform model is used in the theory. A history of previous results on the speed of propagation of the internal disturbances is also given. Existing numerical code based on the Taylor-Goldstein equation is used to validate the applicability of the theoretical model. The results of the experimental investigation are detailed in Chapter 3, where we show that the theoretical predictions support the interpretation of experimental observations. A summary along with suggestions for further investigation are found in the concluding remarks.

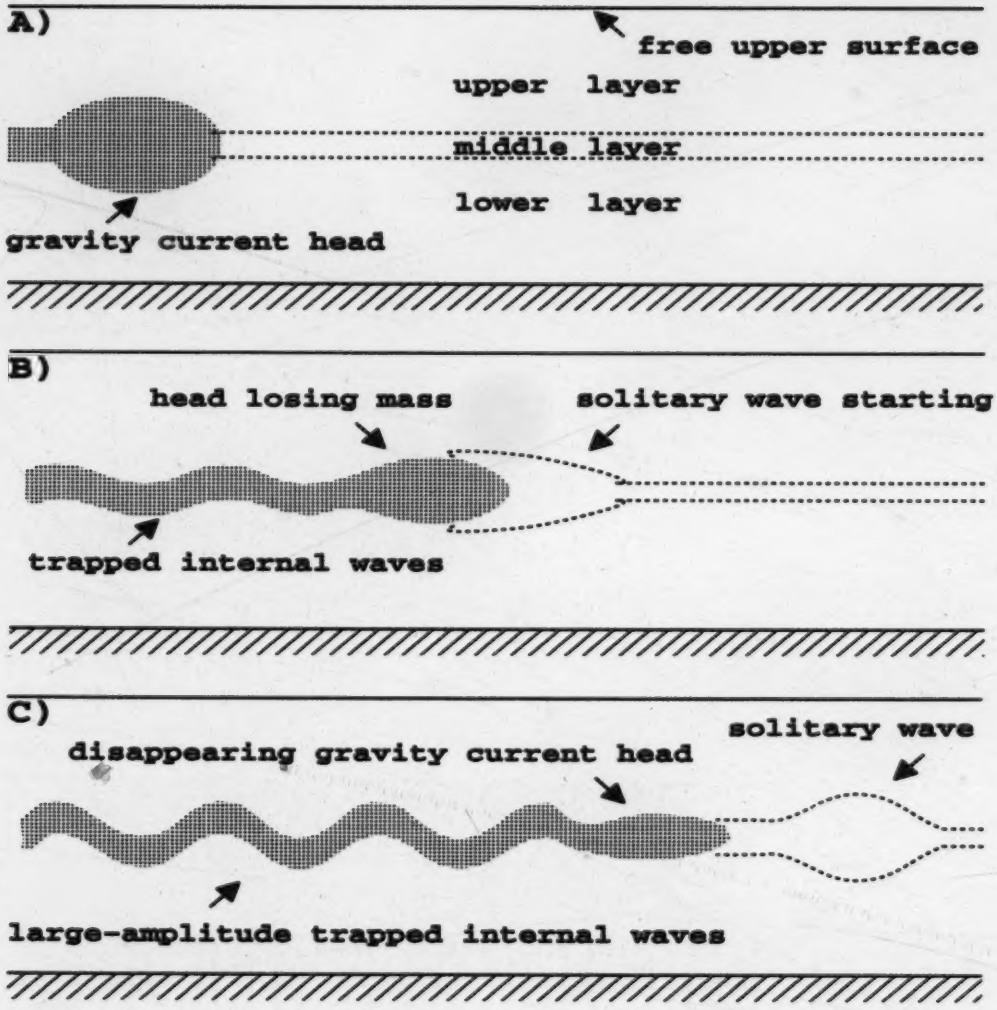

Figure 1.3: Schematic of the main stages of evolution of a gravity current (propagating from left to right) exciting a solitary wave in a three-layer fluid: A) beginning of intrusion, B) size of gravity current head diminishes, trapped internal waves are excited, and a solitary waves starts to form, C) solitary wave separates from diminished gravity current head.

Chapter 2

Theory

To determine the characteristics of trapped internal waves, gravity currents and solitary waves in a three-layer fluid, we focus on a two-dimensional model for simplicity to study the effects of stratification with no background flow. Application of this two-dimensional theory to the experiments is further justified by observing that the flow in the experiments exhibits approximately two-dimensional behaviour. The properties of internal waves, gravity currents and solitary waves are then used to estimate a momentum balance appropriate to the present analytical model.

2.1 The Three-Layer Model

Consider a span-wise uniform three-layer fluid system of infinite horizontal extent as shown in the schematic in figure 2.1, where $2h$ is the depth of the middle layer, $2H$ is the total fluid depth and η_1 and η_2 are the upper and lower interface displacements respectively. The densities of the upper, middle and lower layers are respectively ρ_0, ρ_1 and ρ_2. In many of the theoretical analyses below, the limit $H \to \infty$ is taken. This simplifies the equations and, as will be shown, it is an adequate representation of the experiments. We take the x-direction to be horizontal and the z-direction to be vertical with $z = 0$ half-way through the middle fluid layer. We also assume zero

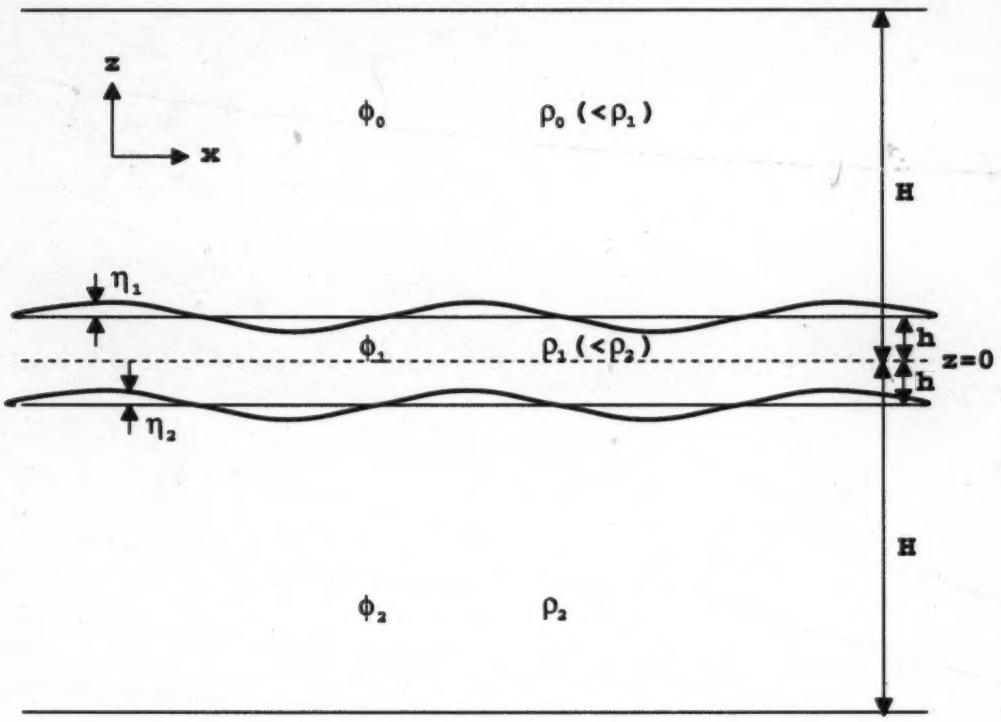

Figure 2.1: Schematic of internal waves in a three-layer fluid system.

surface tension and no diffusion across the interface between the fluids. Assuming the flow in each layer to be inviscid, irrotational and incompressible, we can define velocity potentials ϕ_0, ϕ_1 and ϕ_2 for the upper, middle and lower layers respectively. For the system under investigation, we choose ρ_1 to be the average of ρ_0 and ρ_2, that is, $\rho_1 = \frac{1}{2}(\rho_0 + \rho_2)$. Next, we choose scale parameters ρ_0 and h to define nondimensional variables, denoted below with tildes:

$$\tilde{k} = kh, \quad \tilde{z} = \frac{z}{h}, \quad \tilde{x} = \frac{x}{h}, \quad \tilde{t} = \frac{t}{T}, \quad \tilde{\omega} = \omega T,$$

$$\tilde{\rho_2} = \frac{\rho_2}{\rho_0}, \quad \tilde{\rho_1} = \frac{\rho_1}{\rho_0} = \tfrac{1}{2}(1 + \tilde{\rho_2}),$$

where k is the wave number and ω is the frequency. Here, T is the characterteristic time-scale given by

$$T = \frac{h}{\sqrt{g'h}} = \sqrt{\frac{h}{g'}},$$

where

$$g' = \frac{\rho_2 - \rho_0}{\rho_2} g$$

is the reduced gravity. Gravity is represented nondimensionally by

$$\begin{aligned} \tilde{g} &= g\frac{T^2}{h} = g\frac{h/g'}{h} \\ &= \frac{\tilde{\rho}_2}{\tilde{\rho}_2 - 1}. \end{aligned} \tag{2.1}$$

At this point, we drop the tildes, keeping in mind that the variables and parameters in the governing equations below are nondimensional. The governing partial differential equations for the three-layer system are

$$\begin{aligned} \nabla^2\phi_0 &= 0, \\ \nabla^2\phi_1 &= 0, \\ \nabla^2\phi_2 &= 0, \end{aligned} \tag{2.2}$$

where $\nabla^2 \equiv \frac{\partial^2}{\partial x^2} + \frac{\partial^2}{\partial z^2}$. We assume zero vertical velocity at the upper and lower boundaries. That is, in the limit as $H \to \infty$

$$\frac{\partial \phi_0}{\partial z} \to 0 \quad \text{as} \quad z \to \infty, \tag{2.3}$$

$$\frac{\partial \phi_2}{\partial z} \to 0 \quad \text{as} \quad z \to -\infty. \tag{2.4}$$

Imposing continuous vertical velocity at the upper fluid interface (the interface between the upper two layers of fluid) gives the condition, for small-amplitude displacements,

$$\left.\frac{\partial \phi_0}{\partial z}\right|_{z=1} = \left.\frac{\partial \phi_1}{\partial z}\right|_{z=1} = \frac{\partial \eta_1}{\partial t}. \tag{2.5}$$

Similarly at the lower fluid interface (the interface between the lower two layers of fluid), we have the condition

$$\left.\frac{\partial \phi_1}{\partial z}\right|_{z=-1} = \left.\frac{\partial \phi_2}{\partial z}\right|_{z=-1} = \frac{\partial \eta_2}{\partial t}. \tag{2.6}$$

(Recall that η_1 and η_2 are the vertical displacements of the upper and lower fluid interfaces, respectively, as shown in figure 2.1.) Assuming each interface is a streamline, the Bernoulli condition (with continuous pressure across the interface) for the upper fluid interface is given by

$$\left.\frac{\partial \phi_0}{\partial t}\right|_{z=1} + g\eta_1 = \rho_1 \left.\frac{\partial \phi_1}{\partial t}\right|_{z=1} + \rho_1 g\eta_1. \tag{2.7}$$

For the lower fluid interface, the Bernoulli condition is

$$\rho_1 \left.\frac{\partial \phi_1}{\partial t}\right|_{z=-1} + \rho_1 g\eta_2 = \rho_2 \left.\frac{\partial \phi_2}{\partial t}\right|_{z=-1} + \rho_2 g\eta_2. \tag{2.8}$$

We assume solutions (nondimensional) of the form

$$\eta_1(x,t) = C_1 e^{i(kx-\omega t)}, \tag{2.9}$$

$$\eta_2(x,t) = C_2 e^{i(kx-\omega t)}, \tag{2.10}$$

and

$$\begin{aligned}
\phi_0(x,z,t) &= (A_0 e^{-kz} + B_0 e^{kz}) e^{i(kx-\omega t)}, \\
\phi_1(x,z,t) &= (A_1 e^{-kz} + B_1 e^{kz}) e^{i(kx-\omega t)}, \\
\phi_2(x,z,t) &= (A_2 e^{-kz} + B_2 e^{kz}) e^{i(kx-\omega t)},
\end{aligned}$$

where C_1, C_2, A_0, B_0, A_1, B_1, A_2 and B_2 are coefficients to be determined.

Substituting ϕ_0 into (2.3) and ϕ_2 into (2.4), we find $B_0 = A_2 = 0$, so the above three assumed solutions for velocity potentials reduce to

$$\phi_0 = A_0 e^{-kz} e^{i(kx-\omega t)}, \tag{2.11}$$

$$\phi_1 = (A_1 e^{-kz} + B_1 e^{kz}) e^{i(kx-\omega t)}, \tag{2.12}$$

$$\phi_2 = B_2 e^{kz} e^{i(kx-\omega t)}. \tag{2.13}$$

Substituting η_1, η_2, ϕ_0, ϕ_1 and ϕ_2 (given by (2.9) - (2.13)) into the interface conditions (2.5) - (2.8) gives the following system to be solved:

$$-A_0 k e^{-k} = -A_1 k e^{-k} + B_1 k e^{k} = -C_1 i\omega, \tag{2.14}$$

$$B_2 k e^{-k} = -A_1 k e^{k} + B_1 k e^{-k} = -C_2 i\omega, \tag{2.15}$$

$$-A_0 i\omega e^{-k} + C_1 g = -A_1 \rho_1 i\omega e^{-k} - B_1 \rho_1 i\omega e^{k} + C_1 \rho_1 g, \tag{2.16}$$

$$-A_1 \rho_1 i\omega e^{k} - B_1 \rho_1 i\omega e^{-k} + C_2 \rho_1 g = -B_2 \rho_2 i\omega e^{-k} + C_2 \rho_2 g. \tag{2.17}$$

In matrix form, this is

$$\underbrace{\begin{bmatrix} -ke^{-k} & 0 & 0 & 0 & i\omega & 0 \\ 0 & -ke^{-k} & ke^{k} & 0 & i\omega & 0 \\ 0 & -ke^{k} & ke^{-k} & 0 & 0 & i\omega \\ 0 & 0 & 0 & ke^{-k} & 0 & i\omega \\ -i\omega e^{-k} & \rho_1 i\omega e^{-k} & \rho_1 i\omega e^{k} & 0 & (1-\rho_1)g & 0 \\ 0 & \rho_1 i\omega e^{k} & \rho_1 i\omega e^{-k} & -\rho_2 i\omega e^{-k} & 0 & (\rho_2-\rho_1)g \end{bmatrix}}_{\mathbf{M}} \begin{bmatrix} A_0 \\ A_1 \\ B_1 \\ B_2 \\ C_1 \\ C_2 \end{bmatrix} = \begin{bmatrix} 0 \\ 0 \\ 0 \\ 0 \\ 0 \\ 0 \end{bmatrix}. \tag{2.18}$$

For a nontrivial solution, we must have $\det(M) = 0$. Solving this and letting $\rho_1 = \frac{1}{2}(1+\rho_2)$ (so that g is given by (2.1)), yields the dispersion relations

$$\omega_{\pm}^2 = \frac{\rho_2 k\left\{2\gamma^4(1+\rho_2) \pm \sqrt{4\gamma^8(1+\rho_2)^2 - [(\rho_2-1)^2(1+3\gamma^4) + 16\gamma^4\rho_2](\gamma^4-1)}\right\}}{(\rho_2-1)^2(1+3\gamma^4) + 16\gamma^4\rho_2}, \tag{2.19}$$

where $\gamma \equiv e^k$. We can show that the right-hand side of (2.19) is real and positive for $k > 0$ in order to have real $\omega_{\pm}$. We note that

$$\begin{aligned} 4\gamma^8(1+\rho_2)^2 &= \left[(\rho_2-1)^2(\gamma^4+3\gamma^4) + 16\gamma^4\rho_2\right]\gamma^4 \\ &> \left[(\rho_2-1)^2(1+3\gamma^4) + 16\gamma^4\rho_2\right](\gamma^4-1), \end{aligned}$$

which gives a positive quantity under the square root sign in (2.19). Since the denominator is positive, and the quantity $\rho_2 k$ outside of the braces is positive, we have

established that ω_+ is real. We can also show that ω_- is real since

$$\begin{aligned} 2\gamma^4(1+\rho_2) &= \sqrt{4\gamma^8(1+\rho_2)^2} \\ &> \sqrt{4\gamma^8(1+\rho_2)^2 - [(\rho_2-1)^2(1+3\gamma^4)+16\gamma^4\rho_2](\gamma^4-1)}. \end{aligned}$$

Using (2.1), the coefficients are

$$C_1 = A \text{ (arbitrary)}, \tag{2.20}$$

$$A_0 = \left[\frac{i\omega}{k}\right]\gamma A, \tag{2.21}$$

$$A_1 = \left[\frac{i\omega}{k(1+\rho_2)} - \frac{i\rho_2}{2\omega(1+\rho_2)} + \frac{i\omega}{2k}\right]\gamma A, \tag{2.22}$$

$$B_1 = \left[\frac{i\omega}{k(1+\rho_2)} - \frac{i\rho_2}{2\omega(1+\rho_2)} - \frac{i\omega}{2k}\right]\gamma^{-1} A, \tag{2.23}$$

$$B_2 = \left[\frac{i\omega(1-\gamma^4)}{k(1+\rho_2)} - \frac{i\rho_2(1-\gamma^4)}{2\omega(1+\rho_2)} - \frac{i\omega(1+\gamma^4)}{2k}\right]\gamma^{-1} A, \tag{2.24}$$

$$C_2 = \left[-\frac{(1-\gamma^4)}{(1+\rho_2)} + \frac{k\rho_2(1-\gamma^4)}{2\omega^2(1+\rho_2)} + \frac{(1+\gamma^4)}{2}\right]\gamma^{-2} A. \tag{2.25}$$

Substituting ω_+^2 from (2.19) into (2.25), we can confirm with mathematical software (Maple V Release 5) that C_2 has the same sign as C_1, indicating a sinuous (even) mode as observed in the laboratory experiments (*i.e.*, the upper interfacial waves are in phase with the lower interfacial waves). In addition, we find that $|C_2| \leq |C_1|$. As $k \to 0$ (the long wave limit) we find that $C_2 \to C_1$ as expected, while as $k \to \infty$, $C_2 \to 0$.

Similarly, substituting ω_-^2 from (2.19) into (2.25), we find that C_2 has the opposite sign of C_1, indicating the varicose (odd) mode (*i.e.*, the upper interfacial waves are out of phase with the lower interfacial waves by 180°), and we also find $|C_2| \geq |C_1|$. In the long wave limit, we find that $C_2 \to -C_1$, but for $k \to \infty$, C_2 appears unbounded. However, by an appropriate scaling in terms of C_2, we can show that the limit $k \to \infty$ effectively gives $C_1 \to 0$, that is, the upper interfacial displacement tends to zero.

As the interface thickness h is increased, the nondimensional wavenumber k in-

creases. For large values of h, we can approximate (2.19) by

$$\omega_{\pm}^2 \approx \frac{\rho_2 k\left\{2(1+\rho_2) \pm \sqrt{(\rho_2-1)^2}\right\}}{3(\rho_2-1)^2+16\rho_2}, \tag{2.26}$$

which gives

$$\omega_{+}^2 \to \frac{\rho_2 k}{\rho_2+3} \tag{2.27}$$

and

$$\omega_{-}^2 \to \frac{\rho_2 k}{3\rho_2+1}. \tag{2.28}$$

(Key results from this chapter are listed in table 2.1 in dimensional units.)

In the limit where $k \to 0$ in ω_+ (the sinuous mode dispersion relation for a three-layer fluid of infinite extent) we obtain the familiar dispersion relation for a two-layer fluid of infinite extent, which in dimensional quantities is

$$\omega^2 = gk\frac{\rho_2-\rho_0}{\rho_2+\rho_0} = g'k\frac{\rho_2}{\rho_2+\rho_0}. \tag{2.29}$$

Figures 2.2 and 2.3 shows the dispersion relations and phase speeds respectively for $\rho_1 = 1.02$ (nondimensional) for the infinite-depth model.

For a three-layer fluid of finite extent, the dispersion relation is negligibly different from (2.19) in the regime used in the laboratory experiments where $H = 9$ and $h = 1$, 1.5 and 2 (nondimensional $k \approx 0.3$ to 0.6 .) Figure 2.4 shows phase speeds for the infinite-depth and finite-depth models. Thus, it is valid to approximate the current finite-depth experimental model where $H \gg h$ with an infinite-depth model.

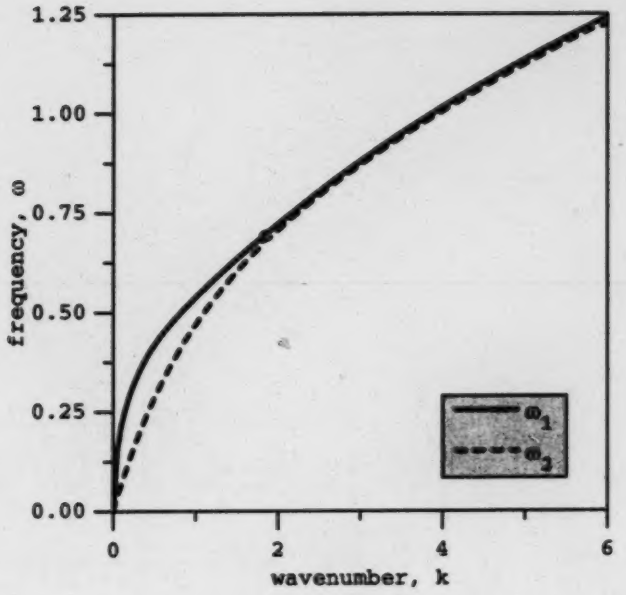

Figure 2.2: Sinuous mode (solid line) and varicose mode (dashed line) dispersion relations for $\rho_1 = 1.02$. Variables and parameters are nondimensional.

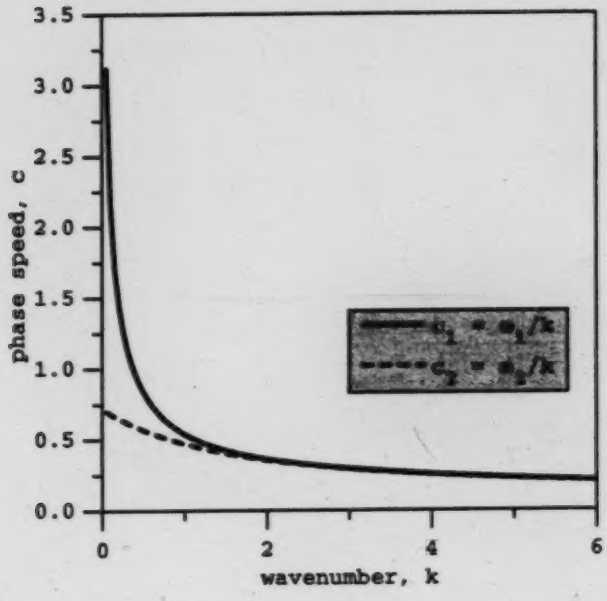

Figure 2.3: Sinuous mode (solid line) and varicose mode (dashed line) phase speeds for $\rho_1 = 1.02$. Variables and parameters are nondimensional.

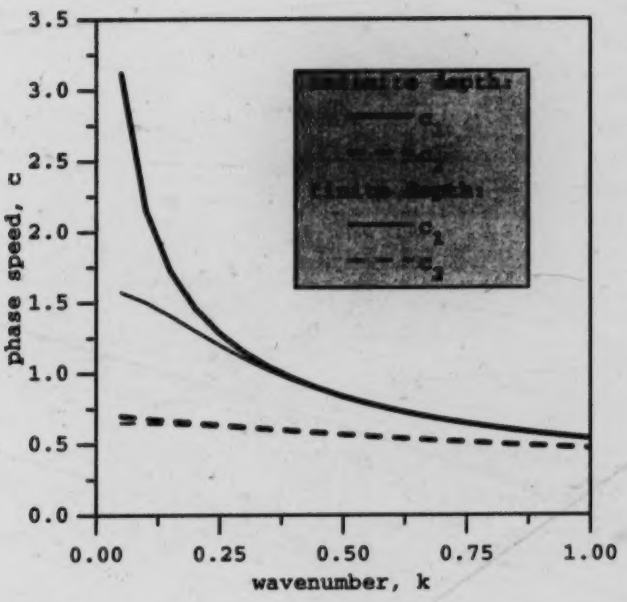

Figure 2.4: Sinuous mode (solid lines) and varicose mode (dashed lines) phase speeds for the infinite-depth model (heavy lines) and finite-depth model (lighter lines) for $H = 9$ and $\rho_1 = 1.02$. Variables and parameters are nondimensional.

2.2 Numerical solutions

In the linear stability analysis of a stratified, incompressible, inviscid fluid, it is customary to define fluctuations of velocity, pressure, and density by small perturbations superimposed on the background flow. That is, for velocity $\mathbf{u} = (u, v, w)$, pressure p and density ρ,

$$\begin{aligned} \mathbf{u}(x,y,z,t) &= \bar{U}(z)\mathbf{i} + \mathbf{u}'(x,y,z,t) \\ p(x,y,z,t) &= \bar{p}(z) + p'(x,y,z,t) \\ \rho(x,y,z,t) &= \bar{\rho}(z) + \rho'(x,y,z,t) \end{aligned}$$

where $\mathbf{i}$ denotes a unit vector in the x-direction. The quantities with an overbar denote mean background flow variables and the primed quantities denote the perturbations. Considering only two-dimensional disturbances (through an application of Squire's Theorem), and assuming that the disturbance is periodic in the direction of flow, we can define a stream function perturbation $\psi(x,z,t) = \varepsilon\phi(z)e^{ik(x-ct)}$, where ε is small, such that

$$u' = -\frac{\partial\psi}{\partial z} \quad \text{and} \quad w' = \frac{\partial\psi}{\partial x}.$$

Substituting these quantities into the basic equations of motion and keeping only lowest order terms, we find that the eigenfunction $\phi(z)$ must satisfy the classical Taylor-Goldstein equation (cf. Drazin & Reid, 1981, p. 324)

$$\phi'' - \left(k^2 - \frac{N^2}{(\bar{U}-c)^2} + \frac{\bar{U}''}{(\bar{U}-c)}\right)\phi = 0 \tag{2.30}$$

for phase speed c and horizontal wavenumber k. Here, $N = (-g\bar{\rho}^{-1}d\bar{\rho}/dz)^{\frac{1}{2}}$ is the buoyancy (Brunt-Väisälä) frequency.

Using numerical code which solves the Taylor-Goldstein equation (Sutherland & Peltier, 1992), we may show that the three-layer infinite-depth model with a discrete stratification is an adequate representation of the finite-depth experiments for which

the density profile is actually continuous over a thin region at the two interfaces between adjacent layers. For a system with zero background shear, (2.30) becomes

$$\phi'' - \left(k^2 - \frac{N^2}{c^2}\right)\phi = 0. \tag{2.31}$$

For a very thin transition region, of thickness T, between adjacent layers, we assume that the density stratification is given by the step-like profile

$$\rho(z) = \rho_1 - \frac{1}{2}(\rho_1 - \rho_0)\left[\tanh\left(\frac{z-h}{T}\right) + \tanh\left(\frac{z+h}{T}\right)\right]. \tag{2.32}$$

Thus, the buoyancy frequency, under the Boussinesq approximation, that is,

$$N^2 = -\left(\frac{g}{\rho(z)}\right)\frac{d\rho}{dz} \approx -\left(\frac{g}{\rho_0}\right)\frac{d\rho}{dz},$$

is given by,

$$N^2 = \left(\frac{-g}{\rho_0}\right)\left(\frac{-\Delta\rho}{2}\right)\left[\mathrm{sech}^2\left(\frac{z-h}{T}\right) + \mathrm{sech}^2\left(\frac{z+h}{T}\right)\right]\left(\frac{1}{T}\right). \tag{2.33}$$

For example, in our experiments typical parameters are $\Delta\rho = 0.02$ g/cm^3, $h = 1$ cm, $T \approx 0.1$ cm and $g \approx 980$ cm/s^2. We then use Sutherland & Peltier's (1992) numerical code to solve (2.31) with N^2 given by the double-sech^2 profile. The bounds of integration reflect the finite-depth fluid used in the experiments (*i.e.*, -9 cm to 9 cm). The dispersion relations for the discrete theoretical model and continuous numerical model for a three-layer fluid are compared in figure 2.5. The corresponding phase speeds are shown in figure 2.6. For k approximately less than 0.25 cm^{-1}, the sinuous mode dispersion relations and phase speeds for the discrete and continuous models fail to correspond. In this region, the finite depth of the fluid in the Taylor-Goldstein code is felt by the long wavelength modes. For $k > 1$, figure 2.5 shows that the curves for the discrete and continuous models for both the sinuous and varicose modes diverge because the thickness of the interfaces is felt by the modes predicted by the Taylor-Goldstein code. However, for the range of k in the experiments (*i.e.*, $k = 0.3$ to 0.6), the theoretical and numerical models show excellent agreement for the sinuous

mode dispersion relation, and good agreement to within 5% for the varicose mode dispersion relation.

Figure 2.6 also shows the phase speed for a two-layer fluid (using (2.29)). For large k, the three-layer phase speeds for both discrete and continuous models asymptote to the two-layer phase speed for an infinite-depth fluid, thus showing sinuous behaviour.

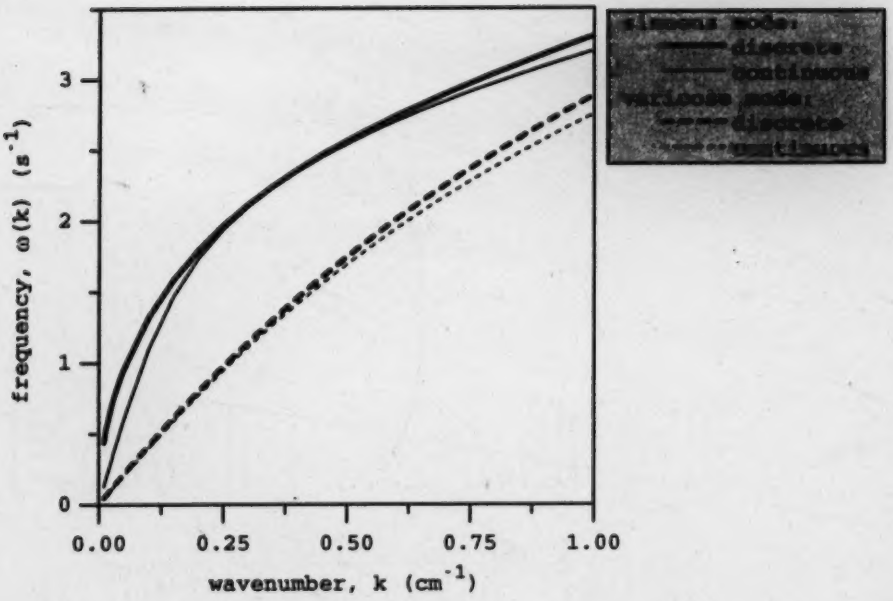

Figure 2.5: Sinuous mode (solid lines) and varicose mode (dashed lines) dispersion relations for the discrete (theoretical) three-layer infinite-depth model (heavy lines) and continuous (numerical) three-layer finite-depth model (lighter lines) for $\rho_1 = 1.02$ g/cm^3.

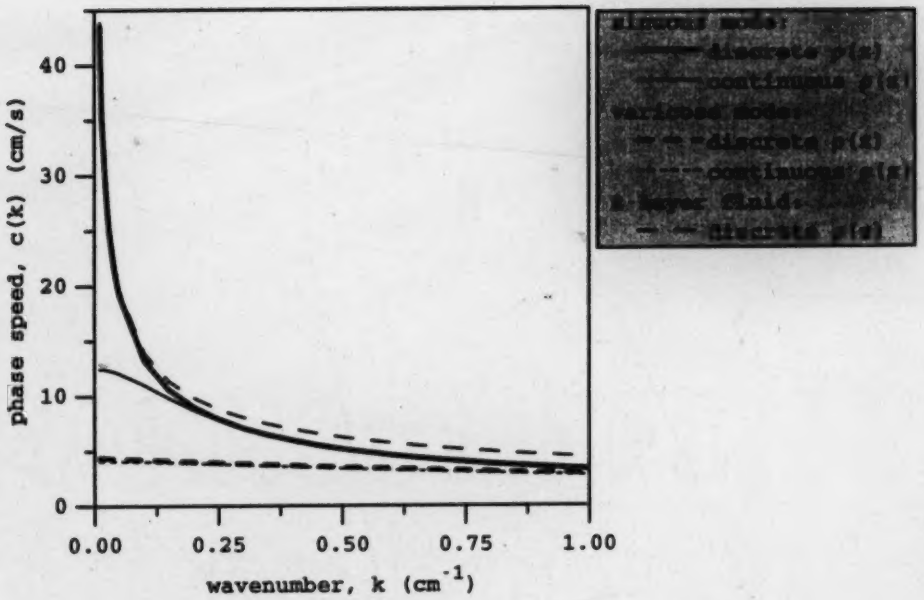

Figure 2.6: Sinuous mode (solid lines) and varicose mode (dashed lines) phase speeds for the discrete (theoretical) three-layer infinite-depth model (heavy lines) and continuous (numerical) three-layer finite-depth model (lighter lines) for $H = 9$ and $\rho_1 = 1.02$ g/cm^3. Also shown is the phase speed for the discrete (theoretical) two-layer infinite-depth model.

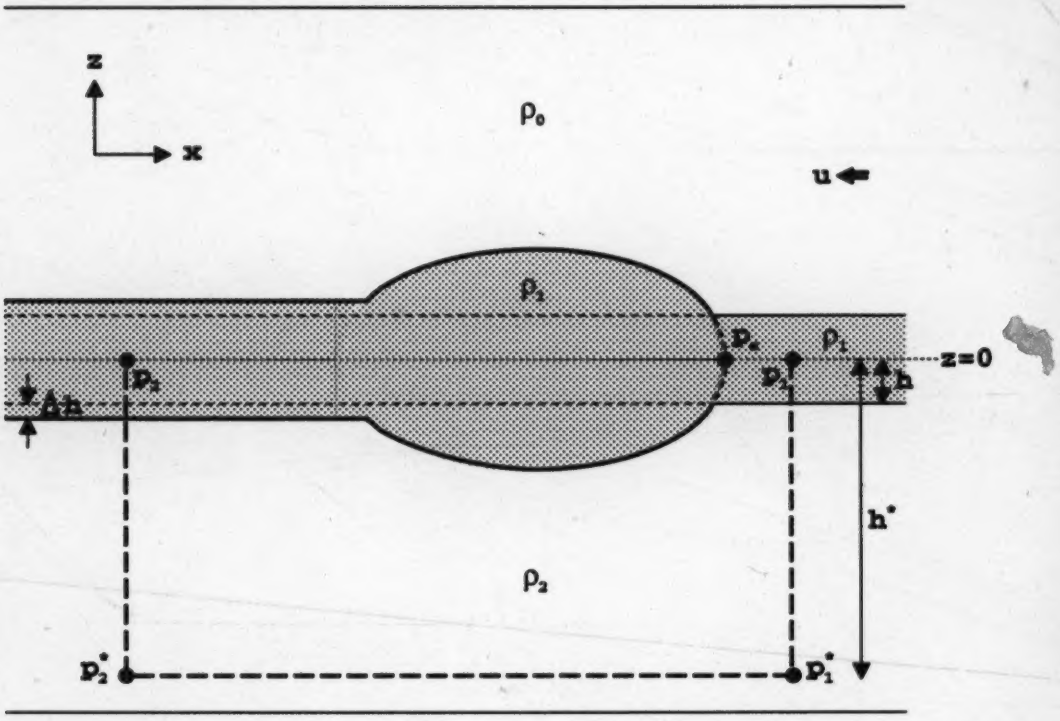

Figure 2.7: Schematic of an intrusive gravity current in a three-layer fluid. The density of the intrusion is the same as the density of the middle layer.

2.3 Speed of the Intrusion

In deriving the propagation speed of an intrusive gravity current in a three-layer fluid, we refer to the schematic in figure 2.7. The density of the intrusion is the same as the density of the middle layer of the three-layer system. It must be noted, that for a gravity current with a density the same as the fluid through which it is intruding, the 'head' is not as well-defined as it would be if the gravity current were not of the same density as the ambient fluid. To simplify the ensuing analysis, we define a head to the gravity current through the middle layer in front of the upper and lower

interfacial displacements as shown in figure 2.7. This allows us to assign a stagnation point at the front of the gravity current head. We choose a reference frame in which the gravity current head is stationary. We consider the case where $\rho_1 = \frac{1}{2}(\rho_0 + \rho_2)$, so that the system is symmetric about $z = 0$, and look at the lower half of the system to calculate the propagation speed of the intrusion. We also assume energy loss due to friction (thus we may not assume that the heavy line in figure 2.7 is a streamline). By Bernoulli's theorem for irrotational, steady flow, we determine the upstream Bernoulli condition to be

$$p_1 = p_s - \tfrac{1}{2}\rho_1 u^2, \tag{2.34}$$

where p_s is the pressure at the stagnation point. We can assume that in an infinitely deep fluid, $p_2 \sim p_s$ since Δh is small compared to the total fluid depth. The points where the pressure is given by p_1^* and p_2^* are far below the intrusion where the flow is assumed to be steady and hydrostatic. Thus, hydrostatic pressure for p_1^* and p_2^* is given by

$$\begin{aligned} p_1^* &= p_1 + \rho_1 g h + \rho_2 g(h^* - h), \\ p_2^* &= p_s + \rho_1 g(h + \Delta h) + \rho_2 g(h^* - (h + \Delta h)). \end{aligned}$$

Far below the gravity current $p_1^* = p_2^*$ so that

$$p_1 = p_s - (\rho_2 - \rho_1) g \Delta h. \tag{2.35}$$

Solving (2.34) and (2.35) gives

$$u_{3layer}^2 = 2\frac{\rho_2}{\rho_1} g' \Delta h, \tag{2.36}$$

where $g' = \frac{\rho_2 - \rho_1}{\rho_2} g$.

From the experimental investigation, we observed that for an intrusion in an ambient fluid with total depth much greater than $(h + \Delta h)$, the disturbance of the free surface was negligible. This observation helps to support the use of the hydrostatic approximation in the current theory.

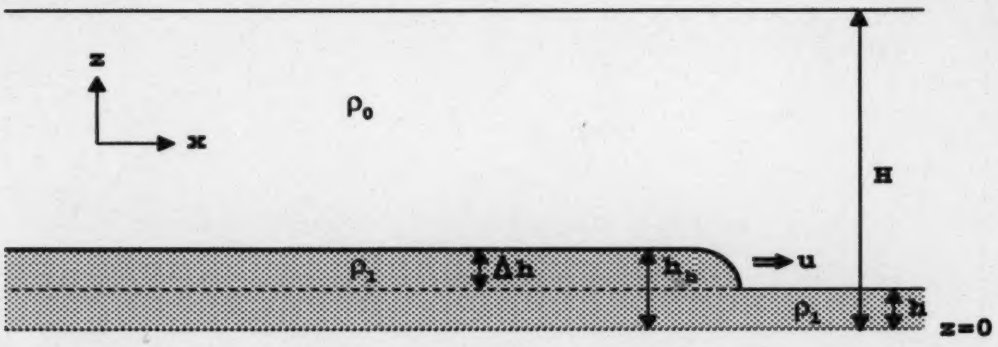

Figure 2.8: Schematic of an internal bore in a two-layer fluid.

For an intrusive gravity current entering a two-layer fluid of infinite extent (figure 2.7 with $h \to 0$), Benjamin (1968) found that

$$u^2_{2layer} = 2g'\Delta h \tag{2.37}$$

for flow with energy loss due to friction. We can see from (2.36) and (2.37) that $u_{3layer} > u_{2layer}$. However, there is no significant difference in the two propagation speeds when $\rho_1 \sim \rho_2$, as in the experimental case.

The possibility that treating the intrusion as an internal jump or bore might provide a more accurate propagation speed was also explored. We simplify the schematic in figure 2.7 and look at only the upper half, $z > 0$ (see figure 2.8). Thus we have a two-layer fluid system for which previous theories have assumed free-slip at the bottom boundary. By symmetry, the results for $z < 0$ should be the same as for $z > 0$, provided the density difference between the upper and middle layer is the same as the density difference between the middle and lower layer, and $\rho_1 \sim \rho_2$. Since the experimental system in this study has no boundary at $z = 0$, the two-layer theories on internal bores should in principle agree with the observed three-layer behaviour.

Internal bores speeds have been derived by Yih & Guha (1955), Wood & Simpson (1984), and more recently by Klemp *et al.* (1997). Details of previously derived speeds for internal bores propagating through a steady two-layer fluid in a channel with rigid

upper and lower boundaries can be found in the paper by Klemp *et al.* (1997), a summary of which is included here. The fluids are assumed to be immiscible. For conservation of momentum, the total flow force must be conserved across the bore, thus the horizontal momentum equation, given by

$$\frac{\partial(\rho v^2)}{\partial x} + \frac{\partial(\rho v w)}{\partial z} + \frac{\partial p}{\partial x} = \frac{\partial \tau_{xx}}{\partial x} + \frac{\partial \tau_{xz}}{\partial z}$$

is integrated over the channel depth H from a point r far downstream the bore front to a point l far upstream. Here, (v, w) are the velocity components in the (x, z)-directions, τ is the turbulent shear stress, and p is the pressure. Far ahead and far behind the bore front, we assume the stress terms vanish, so the result of the integration is

$$\int_0^H \Big(p_r + \rho u^2\Big)\, dz = \int_0^H \Big(p_l + \rho v_l^2\Big)\, dz, \tag{2.38}$$

where u is the speed of the bore. The flow is hydrostatic far upstream and downstream of the bore, that is,

$$\begin{aligned} \frac{\partial p_0}{\partial z} &= -g\rho_0, \\ \frac{\partial p_1}{\partial z} &= -g\rho_1 \end{aligned}$$

in the upper and lower layers, respectively. With mass conservation in each layer and for a uniform velocity downstream, (2.38) becomes

$$\Big[-\frac{h}{h_b} + \sigma\frac{H-h}{H-h_b}\Big](h_b - h)u^2 + \frac{1}{2}g'(h_b^2 - h^2) + \frac{H}{\rho_1}\Big(p_l(H) - p_r(H)\Big) = 0, \tag{2.39}$$

where $\sigma \equiv \frac{\rho_0}{\rho_1}$, h_b is the bore height and $g' = \frac{\rho_1 - \rho_0}{\rho_1} g$. For the intrusive bore depicted in figure 2.8, the classical result for an infinite-depth fluid, taking $H \to \infty$ and $p_l(H) - p_r(H) = 0$, is

$$u^2_{classical} = g' h_b \Big[\frac{h_b + h}{2(h - \sigma h_b)}\Big]. \tag{2.40}$$

The classical result (2.40) for an external bore in a one-layer fluid ($\rho_0 = 0$ and $g' = g$) becomes

$$u^2_{(\sigma=0)} = g' h_b \Big[\frac{h_b + h}{2h}\Big]. \tag{2.41}$$

Yih & Guha (1955) also imposed mass conservation in each layer and overall conservation of momentum. In addition, they related downstream pressure to upstream conditions and, assuming hydrostatic distribution of pressure, approximated the pressure at the fluid interface to be the average of its value far upstream and downstream, that is,

$$\int_r^l p_1(h_1)\frac{\partial h_1}{\partial x}\,dx \simeq \frac{1}{2}\Big[p_l(h_b)+p_r(h)\Big](h_b-h), \tag{2.42}$$

where $h_1(x)$ is the interface height. Neglecting shear and stress terms along the fluid interface, they obtained a solution through a momentum balance within each layer. Combining (2.42) with (2.38) for the upper layer gives

$$p_l(H)-p_r(H)=\frac{-\rho_b(H-h)(h_b-h)}{(H-h_b)[H-\frac{1}{2}(h_b+h)]}u^2, \tag{2.43}$$

where $\rho_b=\rho_0\simeq\rho_1$. Substituting (2.43) into (2.39), and under the Boussinesq approximation assuming the density difference between the two layers is small for the internal bores under investigation, Yih & Guha's (1955) proposed bore speed is given by

$$u_{YG}^2=g'h_b\Big[\frac{(H-h_b)[H-\frac{1}{2}(h_b+h)](h_b+h)}{2hH^2+H(h_b^2-2hh_b-h^2)}\Big]. \tag{2.44}$$

(In the Boussinesq approximation, the influence of density variations on the gravitational force is retained, but the variations are neglected in the fluid inertia.)

Wood & Simpson (1984) assumed that all energy loss occurs in the lower layer. Using the Bernoulli equation across the bore in the upper layer gives the pressure difference as

$$p_l(H)-p_r(H)=\frac{1}{2}\rho_b\Big[1-\frac{(H-h)^2}{(H-h_b)^2}\Big]u^2. \tag{2.45}$$

Substituting (2.45) into (2.39) under the Boussinesq approximation yields Wood & Simpson's (1984) proposed bore speed given by

$$u_{WS}^2=g'h_b\Big[\frac{(H-h_b)^2(h_b+h)}{H(h_b^2+2hH-3hh_b)}\Big]. \tag{2.46}$$

Using experimental data from Simpson & Britter (1979), they also suggested that a bore should not travel faster than a gravity current of the same height h_b. However, Klemp *et al.* (1997) showed that this prevents the use of (2.46) for large ranges of possible bore heights. In a comparative study, Klemp *et al.* (1997) found that (2.44) and (2.46), which assumes energy loss occurs in the lower fluid layer, do not fit the experimental observations of Wood & Simpson (1984) as closely as the theory of Klemp *et al.* (1997), which assumes energy loss in the upper layer. This assumption was based on Benjamin's (1968) proposal that energy is conserved in the lower layer, unlike in classical hydraulic theory (which assumes energy loss occurs in the lower layer). Using the Bernoulli equation across the bore in the lower layer at the bottom of the channel, they obtained the pressure difference

$$p_l(H) - p_r(H) = \frac{1}{2}\rho_b\left[1 - \frac{h^2}{h_b^2}\right]u^2 - g'(h_b - h). \tag{2.47}$$

Substituting (2.47) into (2.39), they found a more accurate internal bore speed to be

$$u^2_{KRS} = g'h_b\left[\frac{h_b(H-h_b)(2H-h_b-h)}{H(h_bH + hH + h_b^2 - 3hh_b)}\right]. \tag{2.48}$$

As $h \to 0$, (2.48) becomes

$$u^2_{B68} = g'h_b\left[\frac{(2H-h_b)(H-h_b)}{H(H+h_b)}\right]$$

which is Benjamin's (1968) result for the propagation speed of a gravity current in a finite-depth fluid, assuming a flow with energy loss. The limit as $H \to \infty$ produces Benjamin's familiar gravity current result for an infinite-depth fluid, $u^2 = 2g'h_b$ (see (2.37)).

For an internal bore in an infinite-depth two-layer fluid, (2.48) yields

$$u^2_{KRS(H\to\infty)} = g'h_b\left[\frac{2h_b}{h_b + h}\right]. \tag{2.49}$$

As $h \to 0$ (or as h_b increases) we obtain (2.37), as expected.

With the previous classical internal bore speed given by (2.40), the limit as $h \to 0$ gives $u^2 = -\frac{1}{2}\frac{\rho_1-\rho_0}{\rho_0}gh_b$, so it is clearly not valid for describing gravity currents. Since

(2.44) and (2.46) both reduce to the classical result (2.41) in the limit as $H \to \infty$, these bore speeds increase without bound in the limit as $h \to 0$ instead of approaching Benjamin's (1968) gravity current speed $\sqrt{2g'h_b}$. Thus, only (2.48) is suited to describe the propagation speed of both internal bores and gravity currents.

The condition under which $u_{KRS(H\to\infty)}$ corresponds exactly with u_{3layer} is found by equating (2.49) to (2.36):

$$\sigma = 1 - \left(\frac{h}{h_b}\right)^2,$$

where $\sigma \equiv \frac{\rho_0}{\rho_1}$. Thus, as the density difference decreases so that $\sigma \sim 1$, we must have $h/h_b \to 0$ for the internal bore speed of Klemp *et al.* to match the three-layer gravity current speed. Figure 2.9 shows the speeds of the two types of intrusions given by (2.49) and (2.36). For $\sigma = 1/1.02$, we find $h/h_b \approx 0.14$ and for $\sigma = 1/1.1$, we find $h/h_b \approx 0.30$.

By comparing the above speeds with typical numbers from experiments, we find that the derived gravity current speed for a three-layer fluid represents the observed data better than the above bore speeds (see figure 3.11), thus confirming that the observed intrusion behaves more like a gravity current than an undular bore.

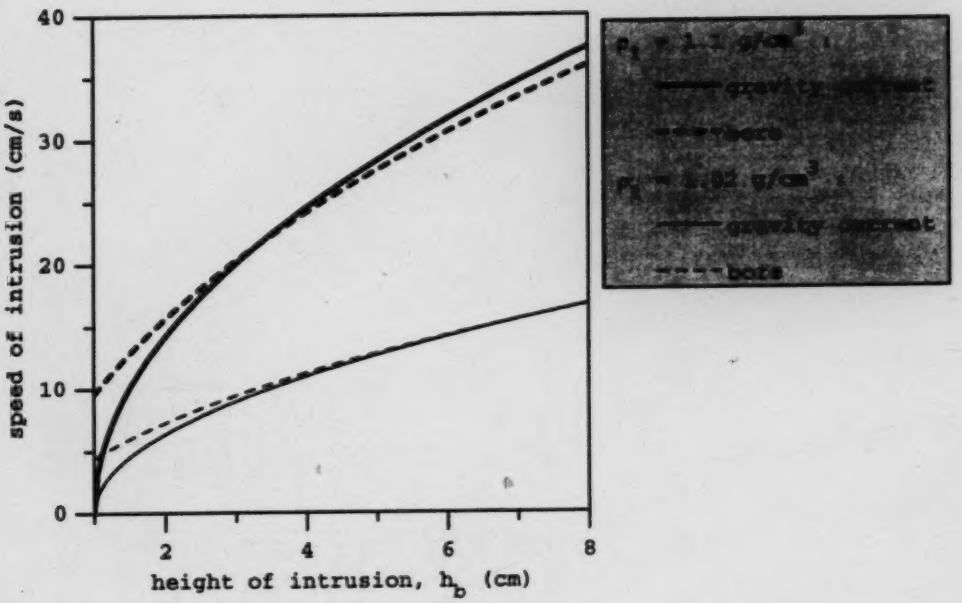

Figure 2.9: Bore speed of Klemp *et al.*, $u_{KRS(H\to\infty)}$, and gravity current speed in a three-layer fluid, u_{3layer}, as a function of intrusion height h_b for $h = 1$ cm. $\rho_0 = 1$ g/cm^3, $g = 1000$ cm/s^2. For $\rho_1 = 1.02$ g/cm^3, speeds match for $h_b \approx 7.1$ cm. For $\rho_1 = 1.1$ g/cm^3, speeds match for $h_b \approx 3.3$ cm.

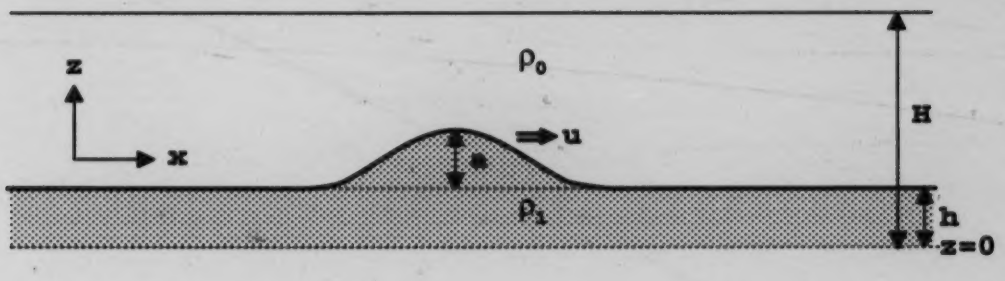

Figure 2.10: Schematic of a solitary wave in a two-layer fluid.

2.4 Speed of the Solitary Wave

Solitary waves in a two-layer fluid (figure 2.10) have been studied theoretically in considerable detail by Keulegan (1953), Long (1956), Benjamin (1966, 1967), Davis & Acrivos (1967), Ono (1975), and Michallet & Barthélemy (1998), to name a few. The internal solitary wave at the interface is an elevated hump when the depth of the upper fluid layer is greater than the depth of the lower fluid layer. It is a depression when the depth of the upper fluid is less than that of the lower fluid. This prediction agrees with the present three-layer fluid experiments, in which the observed double-humped solitary wave is actually two solitary waves, one of elevation at the upper interface and one of depression at the lower interface, propagating at the same speed as depicted in figure 2.11. Interestingly, the two solitary waves in the experiment are observed to remain locked in phase, that is, they are excited simultaneously and they propagate at the same speed.

There have been many theoretical predictions of interfacial solitary wave speeds in these two-layer systems. Two-layer theory which assumes free-slip at the bottom boundary should in principle agree with experimental measurements of solitary wave speed in a three-layer system, where we look at the top half of the system ($z > 0$) and the elevated hump of the double-humped solitary wave. As a starting point for a first order approximation, we use symmetry arguments to reason that for small density

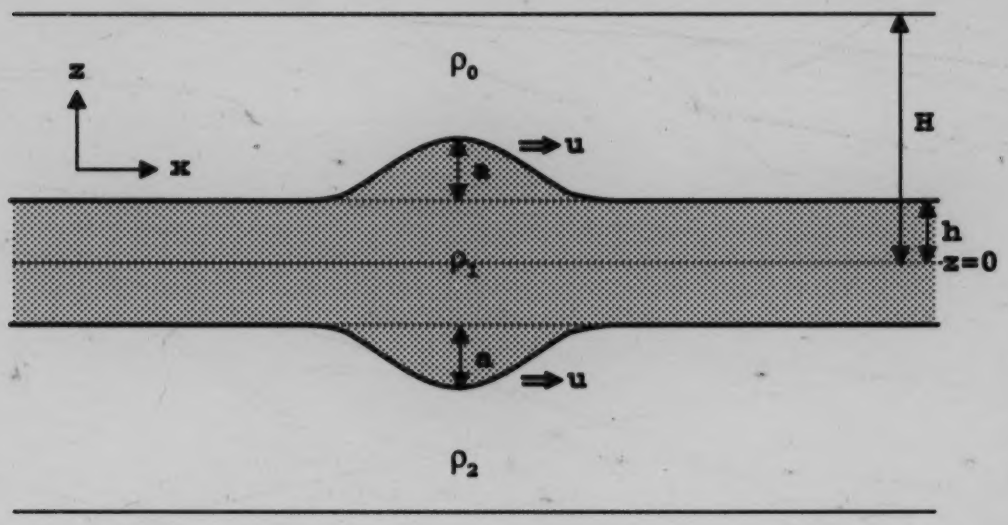

Figure 2.11: Schematic of a double-humped solitary wave in a three-layer fluid where $\rho_1 = \frac{1}{2}(\rho_0 + \rho_2)$.

differences, the solitary wave of depression at the lower interface travels at the same speed as its reflection at the upper interface.

Approximate expressions for a solitary wave on the free surface of shallow water were first formulated by Boussinesq (1871) and Rayleigh (1876). Around twenty years later, Korteweg and de Vries showed that a special solution of their well-known KdV equation is the solitary wave (as given by Boussinesq and Rayleigh), whose profile takes the form

$$f(x) = a\ \mathrm{sech}^2\Big[\frac{(3\frac{a}{h+a})^{1/2}}{2} \cdot \frac{x}{h}\Big],$$

in a reference frame moving with the wave, where a is the maximum amplitude of the solitary wave and h is the depth of the fluid. This sech^2 profile is strictly only correct if $\frac{a}{h} \ll 1$ (cf. Drazin & Johnson, 1989, p. 9). For an interfacial solitary wave, that is, a solitary wave propagating along the interface between two homogeneous fluids, the

profile is modified to

$$f(x) = a\ \mathrm{sech}^2\Big[\frac{(3|R-1|\frac{a}{h})^{1/2}}{2R}\cdot\frac{x}{h}\Big],$$

in the Boussinesq limit, $\rho_0 \sim \rho_1$, where $R = \frac{H-h}{h}$ and H is the total fluid depth. Now h is the depth of the lower layer fluid. For details, see Keulegan (1953), Peters & Stoker (1960) and Christie *et al.* (1978).

The theoretical study of internal solitary waves was initiated by Keulegan (1953) for the special case of a two-layer fluid where $\rho_0 \sim \rho_1$ and the upper liquid was exposed to air at the free surface. The analysis assumed that the two fluids were initially at rest, and the ensuing flow was irrotational. Vorticity at the interface was ignored. The pressure and vertical velocity at the interface was assumed to be continuous and the vertical velocity at the bottom was assumed to vanish. Atmospheric pressure at the free surface was taken to be zero. Neglecting viscosity, Keulegan (1953) assumed the existence of an internal solitary wave which travels long distances without deformation, allowing the transformation $\frac{\partial}{\partial t} = c_K\frac{\partial}{\partial x}$, where c_K is the solitary wave speed, which changes time differentiations to space differentiations. Using scaling arguments in which the vertical velocity and solitary wave height were considered small compared to the lower fluid depth, and assuming that disturbances vanish at infinity, Keulegan (1953) found that the interfacial solitary wave speed is given by

$$c_K^2 = g'h\Big(\frac{H-h}{H}\Big)\Big[1+\frac{a}{h}\cdot\frac{H-2h}{H-h}\Big], \tag{2.50}$$

where $g' = \frac{\rho_1-\rho_0}{\rho_1}g$. In the limit as $H\to\infty$, we find a simpler result

$$c_{(H\to\infty)}^2 = g'h\Big[1+\frac{a}{h}\Big]. \tag{2.51}$$

At lowest order ($a \ll h$) we find the familiar infinitesimal interfacial long-wave speed. We also note that solitary waves are supercritical, that is, the solitary wave speed exceeds the speed of infinitesimal long waves (by an amount proportional to the amplitude of the wave). Equation (2.51) corresponds to the well-known empirical

formula for the speed of propagation of a solitary wave of elevation on a water surface (by setting $\rho_0 = 0$) found by Russell (1844) to be

$$c_R^2 = gh\Big[1 + \frac{a}{h}\Big]. \tag{2.52}$$

The extension of the single-layer KdV model to a two-layer model was also studied by Benjamin (1966), Benney (1966) and Miles (1979). They derived the governing equations for the evolution of internal small-amplitude solitary waves with $\frac{\lambda}{H} \gg 1$ and $\frac{h}{H} = O(1)$. Peters & Stoker (1960) also considered solitary waves in a two-layer fluid with a free upper surface. Keulegan (1953) suggested that the resulting internal solitary wave is approximately independent of whether the upper boundary is free or fixed. In fact, Abdullah (1955) suggested that (2.51) applies to observed atmospheric solitary waves. In deriving a higher order approximation for the speed of a solitary wave in a two-layer system bounded above and below, Long (1956) found that the derived speed to first order was the same as Keulegan's (1953) result for $\rho_0 \sim \rho_1$. Koop & Butler (1981) performed experiments with a free upper surface to show that the KdV extension to a two-layer fluid with a rigid upper boundary is a relevant approximation to describe solitary internal waves where $\frac{a}{H} \ll 1$. Michallet & Barthélemy make a note that this approximation (treating the free surface as fixed) is only satisfactory in the case of a small density difference.

Unlike Keulegan (1953), Benjamin (1966) did not assume $\rho_0 \sim \rho_1$ at the start of his analysis, thus allowing more freedom with the density difference. For the same physical model as in Long (1956), that is, a two-layer fluid with rigid boundaries, Benjamin (1966) used a flow force balance, where the flow force consisted of a horizontal pressure force plus the flux of horizontal momentum, with the method of successive approximations to find an eigenfunction equation. This was solved together with boundary conditions for continuous pressure and vertical velocity at the interface to obtain the speed of the interfacial solitary wave c_{B66}, given by

$$c_{B66}^2 = g'h\Big(\frac{H-h}{H-h+\sigma h}\Big)\Big[1 + \frac{a}{h}\cdot\frac{(H-h)^2 - \sigma h^2}{(H-h)(H-h+\sigma h)}\Big]. \tag{2.53}$$

In the limit where $H \to \infty$ we obtain (2.51). Letting $\sigma \sim 1$ gives Keulegan's result (2.50), and letting $\sigma = 0$ (surface waves) gives Russell's formula (2.52). However, the problem with taking the limit as $H \to \infty$ of c_K and c_{B66} is that the principal assumption in deriving the above speeds, namely that $\frac{h}{H} = O(1)$, is violated. For deep-water theory where $\frac{\lambda}{H} \to 0$ and $\frac{\lambda}{h} \gg 1$, that is, for a two-layer fluid of infinite depth, Benjamin (1967), Davis & Acrivos (1967) and Ono (1975) found that solitary waves with half-width λ have a profile better described by

$$f(x) = \frac{a\lambda}{x^2 + \lambda^2}, \tag{2.54}$$

and that

$$c_{B67}^2 = g'h\left[1 + \frac{3}{4}\frac{a}{h}\right] \tag{2.55}$$

more accurately describes the speed of an interfacial solitary wave (as opposed to the previous classical results for a finite-depth fluid, taking the limit as $H \to \infty$). If the upper surface were free, but the two-layer fluid still had infinite depth, Benjamin (1967) found that changing the upper surface boundary condition from fixed to free yields

$$c_{B67_2}^2 = \frac{\rho_0 - \rho_1}{\rho_0} gh\left[1 + \frac{3}{4}\frac{a}{h}\sigma\right],$$

where h would be the depth of the upper fluid. Christie *et al.* (1978) suggested that Benjamin's speed given by (2.55) is applicable to solitary waves in the planetary boundary layer, whereas the classical result for internal solitary waves (2.51) is better suited to describe the speed of higher altitude waves. Clarke *et al.* (1981) found Benjamin's (1967) theory to agree well with the observed speed of the Morning Glory solitary wave. Ostrovsky & Stepanyants (1989) made observations of solitary waves in shallow seas and found that the classical solitary wave speed described by the KdV model, as in Keulegan (1953), Long (1956) and Benjamin (1966), better suited their study than did Benjamin's (1967) result. This is not so surprising, since the density difference between the fluid layers in the ocean compared with the density

difference between the upper ocean layer and the atmosphere is small enough that the free surface in the observed model can be treated as the rigid boundary used in Long (1956) and Benjamin's (1966) theories.

More recently, Michallet & Barthélemy (1998), assuming that the displacement at the interface is ruled by KdV theory, found that for a two-layer fluid with a free surface

$$c_{MB} = c_0\left[1 + \frac{a}{2h}\left(\frac{\sigma^{-1} - h^2(H-h)/(H'-h)^3}{\sigma^{-1} + h(H-h)/(H'-h)^2}\right)\right] \tag{2.56}$$

with

$$c_0^2 = \frac{gH}{2}\left[1 - \left(1 - \frac{4h(H-h)(\rho_1 - \rho_0)}{\rho_1 H^2}\right)^{\frac{1}{2}}\right] \tag{2.57}$$

and

$$H' = H(1 - \frac{c_0^2}{gH}).$$

For the rigid lid case, they take $H' = H$. Then (2.56) becomes

$$c_{MB_{(rigid)}} = c_0\left[1 + \frac{a}{2h}\left(\frac{\sigma^{-1} - h^2/(H-h)^2}{\sigma^{-1} + h/(H-h)}\right)\right]. \tag{2.58}$$

Letting $\sigma \sim 1$ in (2.58) gives

$$\begin{aligned} c_{MB_{(\sigma\to 1)}} &= c_0\left[1 + \frac{a}{2h}\left(\frac{1 - h^2/(H-h)^2}{1 + h/(H-h)}\right)\right] \\ &= c_0\left[1 + \frac{a}{2h}\left(1 - \frac{h}{H-h}\right)\right] \end{aligned} \tag{2.59}$$

and in the limit as $H \to \infty$ we obtain

$$c_{MB_{(\sigma\to 1, H\to\infty)}} = c_0\left[1 + \frac{a}{2h}\right], \tag{2.60}$$

as found by Abdullah (1956). Now, writing (2.57) as

$$c_0^2 = \frac{gH}{2}\left[1 - \left(1 - \varepsilon\right)^{\frac{1}{2}}\right]$$

and performing a binomial expansion, we obtain

$$c_0^2 = \frac{gH}{2}\left[1 - \left(1 - \frac{1}{2}\varepsilon + \cdots\right)\right]$$

so

$$c_0^2 \approx \frac{gH}{4}\varepsilon = \frac{gH}{4}\left(\frac{4h(H-h)(\rho_1-\rho_0)}{\rho_1 H^2}\right).$$

In the limit as $H \to \infty$, we obtain the familiar linear internal wave speed given by

$$c_0^2 = g'h. \tag{2.61}$$

Combining (2.61) with (2.60) corresponds with (2.51) to $O(\frac{a}{h})$.

In the ensuing analysis, we use Benjamin's (1967) solitary wave speed given by (2.55) since it best suits the analytical model and the laboratory model for the parameter regime used in the experiments.

2.5 Momentum Balance

Using the results of the previous sections in a momentum balance, we may determine a formula for the horizontal distance at which a solitary wave appears. For a balance of horizontal momentum, we show that the initial momentum of the gravity current is equal to that of the trapped internal waves trailing the gravity current head and the solitary wave. That is,

$$M_I = M_{IW} + M_{SW}, \tag{2.62}$$

where M_I is the total momentum at the onset of the intrusion, M_{IW} is the momentum lost to the internal waves and M_{SW} is the momentum of the solitary wave.

We proceed by first estimating the total momentum of the initial intrusion. We define m to be the finite mass of the fluid (with density ρ_1) released from behind a lock to form the intrusive current in a span-wise uniform three-layer fluid. Upon release of the lock, the ambient fluid moves in the direction opposite to that of the intrusion. We assume that approximately half of the total initial kinetic energy, that is, the kinetic energy of the ambient fluid, is transferred to the boundary of the tank (*i.e.*, the boundary behind the lock). This assumption is supported by experimental

data, as will be shown in the next chapter. Thus, $M_I = \frac{1}{2}mv$ is the approximate total momentum of the intrusion, where v is the initial average speed of the intrusion, found using energy considerations. Before the fluid is released, it has available potential energy E_P given by

$$E_P = \int_0^L \int_h^H (\rho_1 - \rho_0)g(z-h)\, dzdx + \int_0^L \int_{-H}^{-h} (\rho_2 - \rho_1)g(-h-z)\, dzdx, \quad (2.63)$$

where L is the length of the lock. For the present experimental system in which the density difference $\Delta\rho$ between the upper two fluid layers and the lower two fluid layers is the same (*i.e.*, $\rho_1 = \frac{1}{2}(\rho_0 + \rho_2)$), (2.63) simplifies to

$$\begin{aligned} E_P &= \int_0^L \int_h^H \Delta\rho\, g(z-h)\, dzdx + \int_0^L \int_{-H}^{-h} \Delta\rho\, g(-h-z)\, dzdx \\ &= (\rho_1 - \rho_0)gL[H^2 - h^2 + 2h(h-H)]. \end{aligned} \quad (2.64)$$

Once the fluid is released, we assume all this available potential energy is converted into kinetic energy E_K. Neglecting losses due to turbulent mixing, $E_K \approx \frac{1}{2}mv^2 = E_P$. If the mass of the intrusion is $2\rho_1 L(H-h)$, then the initial velocity is given by

$$v^2 = g'(H-h). \quad (2.65)$$

Thus the total momentum of the initial intrusion is approximately

$$M_I = \rho_1 L\sqrt{g'(H-h)^3}. \quad (2.66)$$

At a distance d from the lock, the gravity current stops propagating and its momentum is lost to the internal waves and the solitary wave. Using momentum conservation, in the Boussinesq approximation, we find that the momentum extracted by internal waves is

$$\begin{aligned} M_{IW} &\approx \frac{d}{c_{gc}} \cdot \frac{1}{2} \int_{-H}^{H} \rho_1 u u^*\, dz, \\ &= \frac{d}{c_{gc}} \cdot \frac{1}{2}\rho_1 \left[\int_{-H}^{-h} u_2 u_2^*\, dz + \int_{-h}^{h} u_1 u_1^*\, dz + \int_h^H u_0 u_0^*\, dz \right]. \end{aligned}$$

where $c_{gc} = u_{3layer}$ is the speed of the gravity current given by (2.36), $u_i = \frac{\partial \phi_i}{\partial x}$ and u_i^* is the complex conjugate of u_i. Evaluating, we obtain successively

$$
\begin{aligned}
M_{IW} &\approx \frac{d}{c_{gc}} \cdot \frac{1}{2}\rho_1 \Bigg[\int_{-H}^{-h} \left(B_2 e^{kz} \right)^2 (ik) e^{i(kx-\omega t)} (-ik) e^{-i(kx-\omega t)} \, dz \\
&\quad + \int_{-h}^{h} \left(A_1 e^{-kz} + B_1 e^{kz} \right)^2 (ik) e^{i(kx-\omega t)} (-ik) e^{-i(kx-\omega t)} \, dz \\
&\quad + \int_{h}^{H} \left(A_0 e^{-kz} \right)^2 (ik) e^{i(kx-\omega t)} (-ik) e^{-i(kx-\omega t)} \, dz \Bigg] \\
&= \frac{d}{c_{gc}} \cdot \frac{1}{2}\rho_1 k \Bigg[\frac{A_0^2 + B_2^2}{2} (e^{-2kh} - e^{-2kH}) \\
&\quad + (A_1^2 + B_1^2) \sinh(2kh) + 4khA_1B_1 \Bigg] \qquad (2.67)
\end{aligned}
$$

where ω is given by the dispersion relation (2.19). Using (2.21) - (2.24) we find

$$
\begin{aligned}
A_0 &= \left[\frac{i\omega}{k} \right] e^{kh} A, \\
A_1 &= \frac{i}{2} \left[\frac{\omega}{k} \left(\frac{\rho_0}{\rho_1} + 1 \right) - \frac{g'}{\omega} \right] e^{kh} A, \\
B_1 &= \frac{i}{2} \left[\frac{\omega}{k} \left(\frac{\rho_0}{\rho_1} - 1 \right) - \frac{g'}{\omega} \right] e^{-kh} A, \\
B_2 &= \frac{i}{2} \left[\frac{\omega}{k} \left(\frac{\rho_0}{\rho_1} - 1 \right) - \frac{g'}{\omega} - e^{4kh} \left(\frac{\omega}{k} \left(\frac{\rho_0}{\rho_1} + 1 \right) - \frac{g'}{\omega} \right) \right] e^{-kh} A,
\end{aligned}
$$

where A is the maximum vertical displacement by the internal waves of the interface between the upper two fluid layers.

Taking $\xi = f(x) + h$, where $f(x)$ is the vertical displacement of the solitary wave from the interface given by (2.54), and using conservation of mass, the momentum of the solitary wave is

$$
M_{SW} = \int_{-\infty}^{\infty} \int_{-\xi}^{\xi} \rho_1 c_{sw} \left(1 - \frac{h}{\xi} \right) dz dx.
$$

Here, $c_{sw} = c_{B67}$ is the speed of the solitary wave given by (2.55). Evaluating, we obtain successively

$$
\begin{aligned}
M_{SW} &= \rho_1 c_{sw} \int_{-\infty}^{\infty} \int_{-\xi}^{\xi} \left(\frac{\xi - h}{\xi} \right) dz dx \\
&= 2\rho_1 c_{sw} \int_{-\infty}^{\infty} \left(\xi - h \right) dx \\
&= 2\rho_1 c_{sw} \int_{-\infty}^{\infty} f(x)\, dx \\
&= 2\rho_1 c_{sw} \int_{-\infty}^{\infty} \left(\frac{a\frac{\lambda}{2}}{x^2 + (\frac{\lambda}{2})^2} \right) dx \\
&= 2\rho_1 c_{sw} a\pi, \qquad (2.68)
\end{aligned}
$$

where a is the maximum amplitude of the solitary wave. Putting the results (2.66), (2.67) and (2.68) together, we find a formula for d, the horizontal distance from the lock at which we may expect to observe a solitary wave:

$$
d = \frac{2g'\sqrt{2(h_b - h)}\left[L\sqrt{(H-h)^3} - 2a\pi\sqrt{h(1+\frac{3}{4}\frac{a}{h})} \right]}{k\left[\frac{1}{2}(A_0^2 + B_2^2)(e^{-2kh} - e^{-2kH}) + (A_1^2 + B_1^2)\sinh(2kh) + 4khA_1B_1 \right]}. \qquad (2.69)
$$

Here, h_b and A are unknowns. It is interesting to note from (2.69) that d decreases as $1/A^2$. In the next chapter, typical numbers from experiments will be used to investigate the validity of the idealized analytical model for momentum balance. For an easy reference, key formulae in dimensional form are listed in table 2.1.

Dispersion relations corresponding to (2.19) for a three-layer fluid of infinite extent with $\rho_1 = \frac{1}{2}(\rho_2 + \rho_0)$:

$$\omega_{\pm}^2 = \frac{\rho_2 k g^* \left\{ 2\gamma^4(\rho_0+\rho_2) \pm \sqrt{4\gamma^8(\rho_0+\rho_2)^2 - [(\rho_0-\rho_2)^2(1+3\gamma^4) + 16\gamma^4\rho_2\rho_0](\gamma^4-1)} \right\}}{(\rho_0-\rho_2)^2(1+3\gamma^4) + 16\gamma^4\rho_2\rho_0},$$

$$\text{where} \quad g^* = \frac{\rho_2 - \rho_0}{\rho_2} g \qquad \text{and} \qquad \gamma \equiv e^{kh}.$$

Dispersion relations for large h corresponding to (2.27) and (2.28):

$$\omega_+^2 \approx \frac{\rho_2 k g^*}{\rho_2 + 3\rho_0} \qquad \text{and} \qquad \omega_-^2 \approx \frac{\rho_2 k g^*}{3\rho_2 + \rho_0}.$$

Speed of propagation of a gravity current in a three-layer fluid (2.36):

$$c_{gc}^2 = 2g'(h_b - h), \qquad \text{where} \quad g' = \frac{\rho_1 - \rho_0}{\rho_1} g \qquad \text{and} \qquad h_b = \text{height of the current.}$$

Klemp *et al.*'s (1997) speed of propagation of an internal bore in a deep fluid (2.49):

$$c_{bore}^2 = g' h_b \left[\frac{2h_b}{h_b + h} \right], \qquad \text{where} \quad h_b = \text{height of the bore.}$$

Benjamin's (1967) speed of propagation of an interfacial solitary wave in a deep fluid (2.55):

$$c_{sw}^2 = g' h \left[1 + \frac{3}{4}\frac{a}{h} \right], \qquad \text{where} \quad a = \text{amplitude of the solitary wave.}$$

Components of the momentum balance, (2.66), (2.67) and (2.68):

$$M_I = \rho_1 L \sqrt{g'(H-h)^3},$$

$$M_{IW} = \frac{d}{c_{gc}} \cdot \frac{1}{2}\rho_1 k \left[\frac{A_0^2 + B_2^2}{2}(e^{-2kh} - e^{-2kH}) + (A_1^2 + B_1^2)\sinh(2kh) + 4khA_1B_1 \right],$$

where d = distance at which the solitary wave appears,

$$M_{SW} = 2\rho_1 c_{sw} a \pi.$$

Table 2.1: Key formulae in dimensional units.

Chapter 3

Experimental Observations

Experiments of intrusions in two- and three-layer fluids were carried out in which the densities of the layers and the thickness of the middle layer (in the three-layer case) were varied. It will be shown that theory from the previous chapter supports the interpretation of experimental results.

3.1 Experimental Procedures

In a series of initial experiments, a three-layer fluid was found to be created by an intrusion into a two-layer fluid. The glass tank used was 197 cm long, 17.5 cm wide and 48.5 cm tall, but for the experiments it was only filled to a total depth of 18 cm. In making a two-layer fluid, the tank was first filled to a depth of 9 cm with salt water of a predetermined density ρ_2. A second layer of fresh water ($\rho_0 \approx 1$ g/cm^3) was carefully added through a sponge float (a raft with styrofoam walls and a sponge base) which minimized mixing between the two different layers. The depth of this second layer was also 9 cm. At one end of the tank a conductivity probe was placed in the fluid and density measurements were taken at various depths to determine the density stratification. 10 cm from the other end, a water-tight gate was inserted in between two thin glass strips forming a vertical guide from which the gate could

be rapidly extracted. The fluid behind the gate was thoroughly mixed to create a homogeneous fluid with density $\rho_1 = \frac{1}{2}(\rho_0 + \rho_2)$, the mean of the upper and lower densities. 50 drops of fluorescene (a fluorescent yellow dye) were added so the mixed fluid could be easily distinguished from the ambient fluid after the gate was removed. Once the large scale motions from the mixing had died down, the intrusion was formed by rapidly extracting the gate. The fluid from behind the gate formed a gravity current which propagated along the interface between the two ambient layers. Trailing the gravity current were trapped internal waves. These were of relatively small amplitude and persisted for only one or two wavelengths. After the fluid settled, density measurements revealed in general that the mixing resulted in a three-layer fluid in which the middle layer resulting from the intrusion had density ρ_1.

The intrusion was recorded on a video camera focusing on a 20 cm wide window of the tank extending between 80 cm and 100 cm from the lock. The DigImage software package, running on a PC, was used to take velocity, wavelength, amplitude, and various other length measurements from digitized images of the video recording.

The lock-release step to this point in the experimental procedure was labelled as one 'run'. After half an hour had elapsed (sufficient time for the wave motion to dissipate), the process was repeated: the new density profile was determined using the conductivity probe (and thus the thickness of the new interfacial layer), the lock was inserted into the guides again, the fluid behind the lock was mixed and dyed a new colour and the lock was released. Typically, on the fifth run, the gravity current intruding through the interfacial layer was observed to excite a double-humped solitary wave, also appearing in the interfacial layer in front of the gravity current head. This double-humped solitary wave was in fact two solitary waves, one of elevation at the upper interface and one of depression at the lower interface, propagating together in phase. Upon the creation of the solitary wave, the gravity current in turn stopped propagating. Trailing the gravity current were trapped internal waves. For a sufficiently thick interfacial layer, we propose that this transition to a solitary wave

occurs when the gravity current resonantly couples with the trapped internal waves that extract momentum from the gravity current head. Typical photographs of the intrusion at different times during the first and fifth run of an experiment are shown in figure 3.1.

The amplitude of the internal waves was measured from an intensity enhanced vertical time series obtained from the digitized recording of the waves passing through the window on which the camera was focused. The vertical time series was taken 80 cm from the lock. The average amplitude was found by measuring half the vertical distance from a crest to the next trough in images such as those shown in figure 3.2. Likewise, the speed of the gravity current head and the first trailing internal wave along with the wavelength measurements were obtained from a horizontal time series such as that shown in figure 3.3. Speeds were measured by calculating the slopes of the diagonal bars in the time series, and the wavelength was determined by measuring the horizontal distance between the top of two adjacent diagonal bars (the peak to peak distance).

In some instances, the density profiles of these experiments indicated a significant amount of mixing at the interfaces between the adjacent layers, giving a continuous stratification. The mixing was a result of the entrainment from the Kelvin-Helmholtz billows appearing behind the gravity current head. To keep the system discretely stratified, the experimental procedure was revised so that the initial intrusion propagated into a three-layer fluid, thus allowing a more direct comparison with the three-layer theory from the previous chapter. Several experiments were performed in which the thickness of the interfacial (middle) layer, $2h_i$, and the middle and lower layer densities (and thus the density difference, $\Delta\rho$) were varied. The middle layer of density $\rho_1 = \frac{1}{2}(\rho_0 + \rho_2)$ was added on top of the lower layer through a sponge float to a depth of $2h_i$, after which a layer of fresh water was added on top of the middle layer in a similar manner (see figure 3.4). In each experiment, the total fluid depth was $2H = 18$ cm, with the upper and lower layers having equal depth, $H - h_i$. The rest

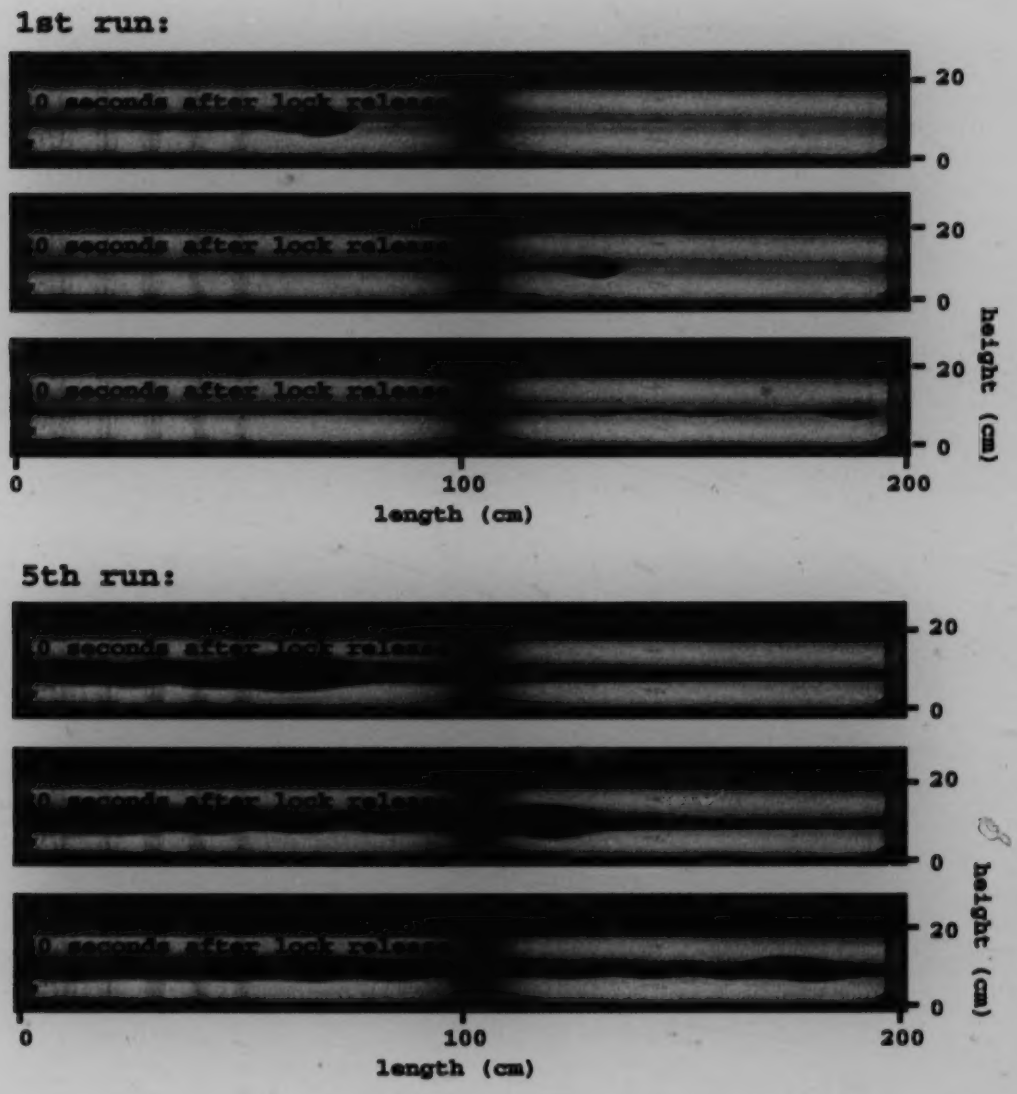

Figure 3.1: Typical photographs of the intrusion at different times during the first and fifth run of an experiment in which the initial ambient fluid consists of two homogenous layers of different densities.

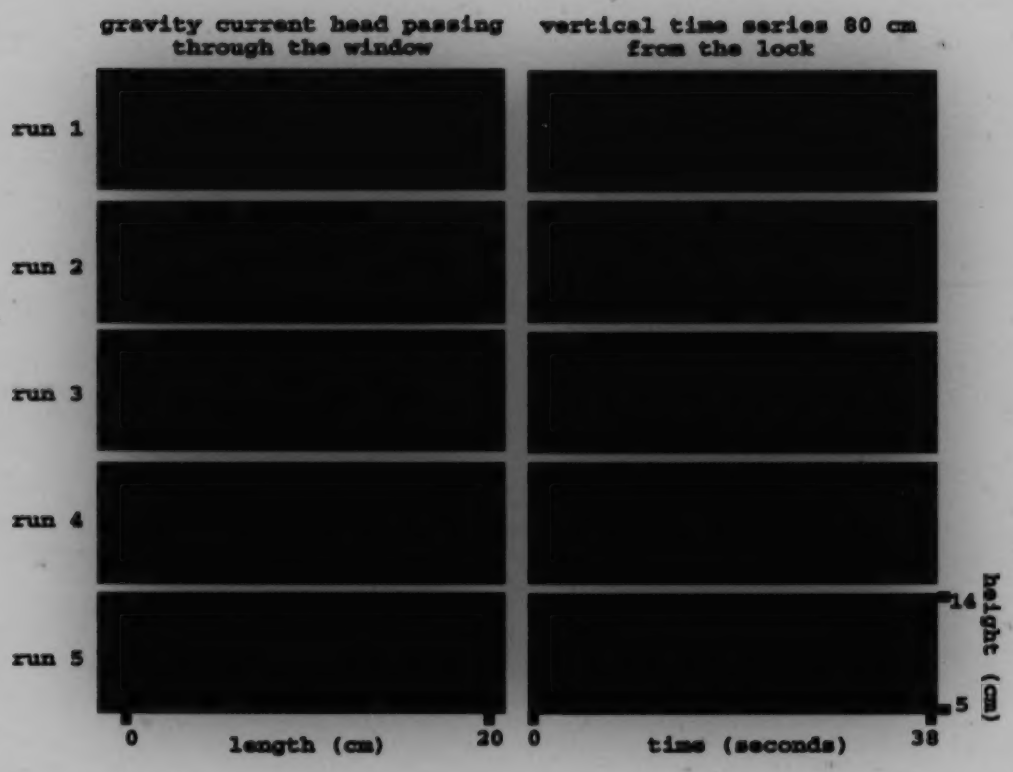

Figure 3.2: Digitized images of the gravity current head passing through the camera's focus (the 'window') and vertical time series for each run of an experiment with $\Delta\rho = 0.05$ g/cm^3.

of the experimental procedure remained the same: the density profile was obtained, the gate was inserted into the guides, the fluid behind the gate was mixed so that it was of uniform density ρ_1, and the gate was released (see figure 3.5).

Table 3.1 shows a checklist of the experiments performed. For experiments with $2h_i = 2$ cm, four runs were carried out before emptying the tank for a new experiment. Only one intrusion was generated for each of the experiments with $2h_i = 3$ and 4 cm since a solitary wave was observed on the first run.

Figures 3.6 and 3.7 show the different density profiles for a two-layer setup with an

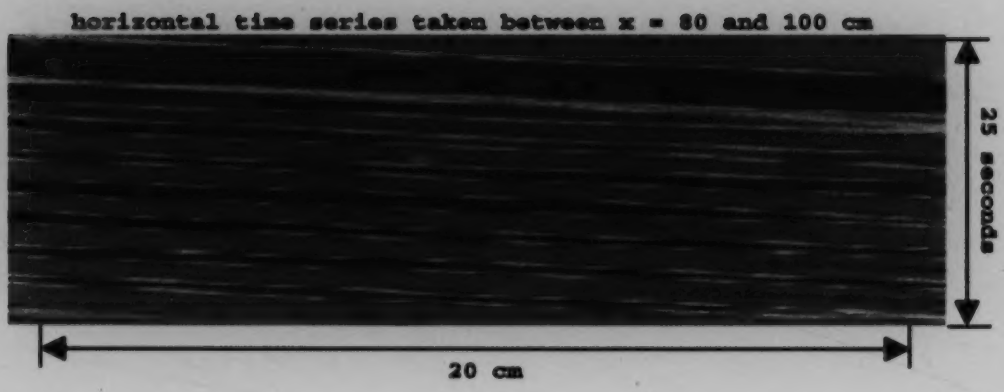

Figure 3.3: Horizontal time series for the fourth run of an experiment with $2h_i = 2$ cm and $\Delta\rho = 0.05$ g/cm^3.

intrusion and the revised three-layer experiment. In the experiment corresponding to figure 3.7, the density of the lower layer was chosen to be 1.02 g/cm^3 and, in keeping the density difference $\Delta\rho$ constant between adjacent layers, the density of the interfacial layer was chosen to be 1.01 g/cm^3. Errors in the calibration of the conductivity probe, design flaws in the probe tip and the roughness of the data collected from the voltmeter (to which the probe was connected) resulted in unreliable probe data giving large error margins. However, the errors were systematic enough that the data compiled for figures 3.6 and 3.7 display a difference, if only qualitative, in the roughly step-like density profiles of the two- and three-layer fluids. More reliable measurements of density profiles taken by Sutherland (unpublished) clearly show that a two-layer fluid becomes a three-layer fluid after repeating the lock-release experiments several times.

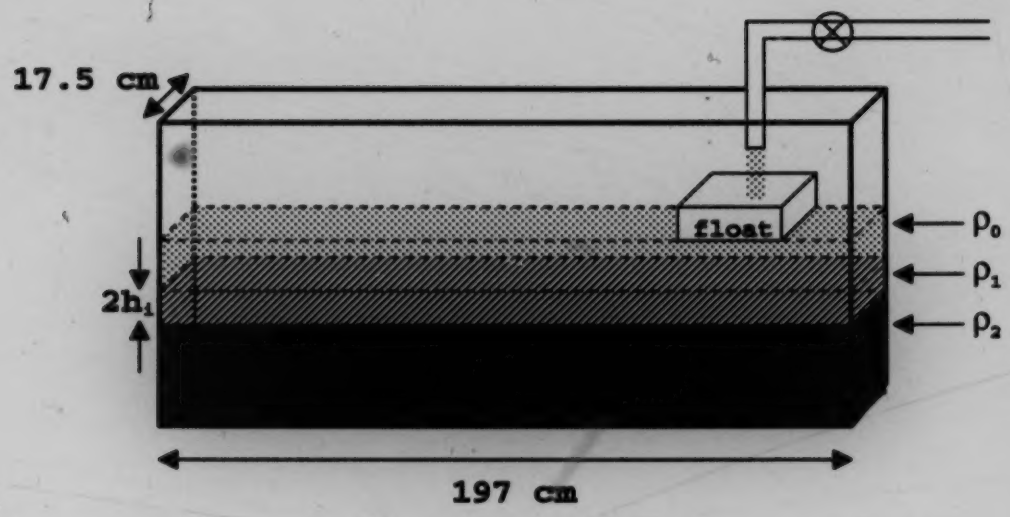

Figure 3.4: Schematic of the three-layer fluid experimental setup.

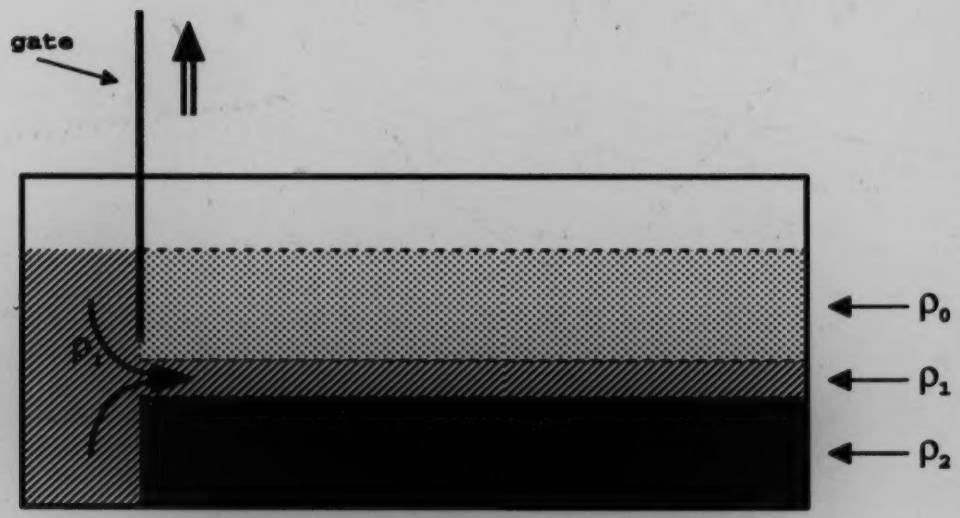

Figure 3.5: Schematic of a lock-release in three-layer fluid (front view). The fluid behind the lock has the same density as the interfacial layer.

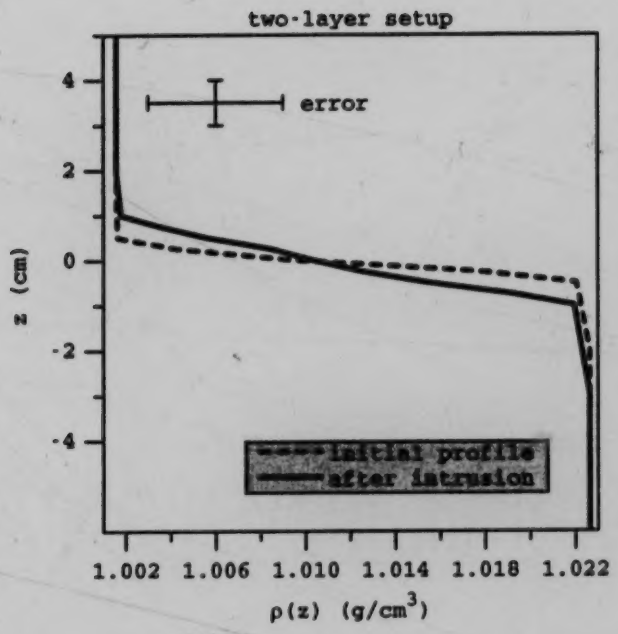

Figure 3.6: Initial density profile for a two-layer fluid (dashed line) and a density profile of the same fluid after an intrusion (solid line). The intrusion creates a new interfacial layer which is continuously stratified.

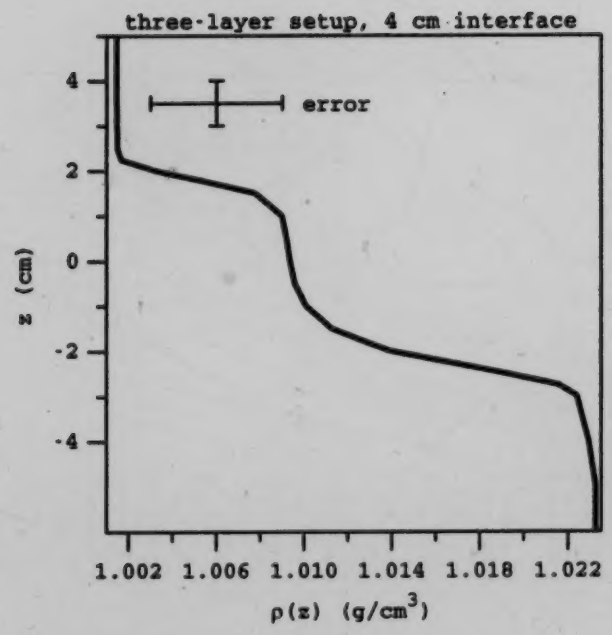

Figure 3.7: Initial density profile for a three-layer fluid with $2h_i = 4$ cm. The step profile resembles a discrete stratification.

ρ_1 (g/cm^3)	ρ_2 (g/cm^3)	$2h_i$ = 2 cm	$2h_i$ = 3 cm	$2h_i$ = 4 cm
1.0025	1.005	✓	✓	✓
1.005	1.01	✓		✓
1.01	1.02	✓	✓	✓
1.02	1.04	✓	✓	✓
1.03	1.06	✓	✓	✓
1.04	1.08	✓		✓
1.05	1.1	✓		✓

Table 3.1: Checklist of experiments performed.

3.2 Observations

Unless otherwise indicated, the laboratory observations and data used in this section represent the series of experiments with an initial three-layer stratification.

Upon release of the lock, the intruding fluid emerging from behind the partition takes the form of a gravity current head with trailing trapped internal waves. In the case of a two-layer fluid, the trapped internal waves behind the gravity current are of small amplitude, decaying rapidly with each period, so that they are only sustained for a few periods before disappearing. The behaviour of the internal waves in a three-layer fluid is quite different: the trapped internal waves at the upper and lower interface resonantly couple with each other, thus producing large-amplitude waves, which are sustained for a longer time. (They are still sustained upon return of the reflected current, showing only a slight attenuation of amplitude due to viscosity.)

In a given setup, the Kelvin-Helmholtz billows appearing behind the gravity current head become less visible for each lock release due to mixing at the interface between adjacent fluid layers from the previous intrusion. We observe that these instabilities behind the head diminish as the interface thickness increases from $2h_i = 2$ cm

$\Delta\rho$ (g/cm^3)	Average amplitude (cm)			
	run 1	run 2	run 3	run 4
0.01	0.2	0.3	0.3	0.4
0.02	0.3	0.3	0.4	0.5

$2h_i$ = 2 cm

Table 3.2: Average amplitude (± 0.05 cm) in each run for two experiments ($\Delta\rho = 0.01$ and 0.02 g/cm^3) with $2h_i = 2$ cm.

to $2h_i = 4$ cm for given ρ_2 and ρ_1. This relation between the instability size and interface thickness was also observed by Britter & Simpson (1981) in their two-layer experiments. They varied the interface thickness by allowing the two ambient fluids to diffuse over a period of time, and observed that the Kelvin-Helmholtz billows reduced in size as the interface thickness was increased. We also observe that the Kelvin-Helmholtz billows appearing behind the gravity current head increase in size for a faster gravity current which exhibits greater velocity shear at the interface between the gravity current head and the ambient fluid (cf. Simpson, 1997, p. 147). This is a direct affect of the density difference, $\Delta\rho$, between two adjacent layers (Thorpe, 1971), since the speed of propagation of the gravity current head (as given by 2.37) is directly proportional to the square root of the density difference (Benjamin, 1968).

The mass associated with the gravity current head is noticeably reduced due to mixing, which in turn is affected by the internal waves. Since the gravity current propagates at approximately constant speed through the interfacial layer, the momentum of the current must decrease. Assuming that the vertical transport of momentum is negligible, momentum must be conserved in the system. The loss of momentum from the gravity current is accounted for, in part, by the generation of the trailing internal waves. For a given initial stratification with $2h_i = 2$ cm, the average amplitude (over eight periods) of the internal waves increases for each run (see table 3.2). This corre-

sponds to a greater momentum loss from the gravity current head as the interfacial layer thickens. At a sufficient interfacial layer thickness a solitary wave is excited, generally on the fourth run if $2h_i = 2$ cm. (Whenever a fifth run was carried out, the solitary wave was excited at a distance along the tank closer to the lock, as predicted by (2.69).) Smaller amplitudes in experiments with smaller $\Delta\rho$ are observed, possibly due to the smaller amount of available potential energy before the lock is released (according to (2.64), potential energy $E_P \propto \Delta\rho$). In addition, because the number of waves behind the gravity current head is roughly the same, there is a smaller portion of the gravity current's momentum transferred to the internal waves for stratifications with a smaller density difference (see table 3.7). Thus there is sufficiently large momentum left over in the gravity current head to excite a solitary wave at a distance closer to the lock (see table 3.6). These tables will be discussed in further detail at a later stage.

For a two-layer setup the amplitude in the first two runs is observed to decay rapidly with each period. This decay is more noticeable for a smaller density difference, for example, when $\Delta\rho \approx 0.008$ and 0.005 g/cm^3.

The average wavelength of the internal waves varies by a small amount for different interfacial layer thickness. For $2h_i = 4$ cm, $\lambda = 21 \pm 0.5$ cm, for $2h_i = 3$ cm, $\lambda = 20 \pm 0.5$ cm, and for $2h_i = 2$ cm, $\lambda = 19 \pm 0.5$ cm. These wavelengths correspond to $kh \approx 0.6$, 0.5 and 0.3 respectively.

Figure 3.8 shows the theoretical frequency (using the sinuous mode of (2.19)) as a function of the density difference $\Delta\rho$ (nondimensional) for three different values of kh along with observed values for ω (nondimensional). These nondimensional quantities are given by

$$\begin{aligned} \omega \text{ (nondimensional)} &= \omega T = \omega\sqrt{\frac{h}{g'}} \\ \Delta\rho \text{ (nondimensional)} &= \frac{\Delta\rho}{\rho_0}. \end{aligned}$$

For the three curves shown, the measured frequency collected from the set of experi-

ments with approximately the same value of kh always lies under the theoretical curve by about 0.05 (using the nondimensional units in figure 3.8). The difference in frequency between pairs of data, as determined by a least squares fit exhibit comparable vertical spacing to the theoretical curves in figure 3.8. The slope of the least squares fit is approximately 0.07 for $kh = 0.3$ and 0.5, and approximately 0.2 for $kh = 0.6$. The continuous stratification, nonlinearity and friction in the experiments may hold some responsibility for the discrepancy between the experimental observations of frequency (and phase speed) and the theoretical curves produced for a discrete stratification. Figure 2.5 shows that the frequency of the waves in the continuously stratified case is lower than the frequency of the waves in the discretely stratified case.

It is also apparent from figure 3.9 that as the interfacial layer thickness increases, the observed frequency increases. For $\Delta\rho$ (nondimensional) = 0.02, figure 3.9 shows the dispersion relation as a function of the wavenumber with observations from experiments with different interfacial layer thickness. Intuitively, this relationship between the frequency and interfacial layer thickness is predicted by shallow water theory: the speed of the internal waves can be approximated by $c = \sqrt{g'h}$, thus the dispersion relation is $\omega = k\sqrt{g'h}$. As h increases, so does ω. More accurately, for waves at the interface of two incompressible, irrotational, inviscid fluids of finite depth, it can be shown that the dispersion relation (in dimensional form) is given by

$$\omega^2 = gk\left(\frac{\rho_0 - \rho_1}{\rho_1 \coth(kh) - \rho_0 \coth(kh_0)}\right), \tag{3.1}$$

where h_0 and h are the depths of the upper and lower layers respectively, and ρ_0 and ρ_1 are the densities of the upper and lower layers respectively. In the special case where $h_0 \to \infty$ and $kh \ll 1$ (*i.e.*, shallow water theory) and $\rho_0 \ll \rho_1$, (3.1) becomes

$$\omega^2 = k^2 g' h, \tag{3.2}$$

where $g' = \frac{\rho_1 - \rho_0}{\rho_1} g$. From (3.2) we see that the frequency increases as h increases, as observed in the experiments.

$\Delta\rho$ (g/cm^3)	Gravity current head speed (cm/s)			
	run 1	run 2	run 3	run 4
0.005	3.2	3.1	3.1	2.9
0.01	4.7	4.6	4.0	3.7
0.02	5.3	5.0	4.9	4.6
0.04	7.5	7.9	7.5	6.7

$2h_i = 2$ cm

Table 3.3: Gravity current head speeds (± 1 cm/s) in four runs for an initial set up with $2h_i = 2$ cm.

For experiments with $2h_i = 2$ cm, we observe the gravity current head speed to change from one run to the next for a given initial stratification. The data given in table 3.3 indicate a general trend for the gravity current head speed to decrease moderately on each run of an experiment, as repeated mixing causes the interface thickness to increase (see figure 3.10), which causes the upper and lower layers thicknesses to decrease. Thus, Benjamin's (1968) theory would predict a slower gravity current upon each run of an experiment. This, along with the diminished size of the gravity current head, is perhaps another indication of momentum lost to the internal waves, which grow in amplitude for each run. We can also see in figure 3.10 that the gravity current head speed increases as $\Delta\rho$ is increased, which agrees with the prediction from the theoretical speed (2.36), $u_{3layer} = \sqrt{2g'\Delta h}$ proposed in the previous chapter. (Recall that Δh is half of the difference between the initial interfacial layer thickness and the interface thickness behind the intrusion.) Table 3.4 lists observed gravity current head speeds (the initial intrusion) in experiments with $2h_i = 2$ cm, the theoretical speed of a gravity current and the bore speed (2.49) of Klemp *et al.* (1997), $u_{KRS(H\to\infty)} = \sqrt{g'h_b(\frac{2h_b}{h_b+h})}$, where h_b is the observed height of the gravity current head. Figure 3.11 compares the observed data for the first run of experiments

$\Delta\rho$ (g/cm^3)	Gravity current head speed (cm/s)		
	observed	u_{3layer}	$u_{KRS(H->\infty)}$
0.005	3.2	1.8	3.9
0.01	4.7	3.8	6.3
0.02	5.3	6.6	9.3
0.04	7.5	9.7	11.7

$2h_1$= 2 cm

Table 3.4: Gravity current head speeds (± 1 cm/s) of the first run for experiments with $2h_i = 2$ cm, and predicted speeds from theory.

with $2h_i = 2$ cm to the speeds given by (2.36) and (2.49). As mentioned earlier, the theoretical gravity current speed better predicts the observed gravity current speed. A finite mass for the intrusion was not assumed in the theoretical bore speed of Klemp *et al.* (1997), thus it does not adequately represent the observed speeds for intrusions of finite mass.

The phase speed of the first trailing internal wave behind the gravity current head is observed to be generally faster than the gravity current head speed. Table 3.5 shows the gravity current head speed and the first trailing internal wave speed for experiments with $2h_i = 2$ cm. Most measured phase speeds are within 0.5 cm/s of the gravity current speeds. However, figure 3.10 shows that no obvious trend could be observed in the change of the phase speed from one run to the next in a given experiment. These variations could be caused by a number of factors: the Kelvin-Helmholtz instabilities behind the gravity current head may interfere with the trailing internal wave, the superposition of the trailing internal wave could act to create spurious fluctuations in the measured phase speed, the motion due to mixing prior to the lock fluid's release may also disturb the system, or the motion of the lock being released may generate internal waves, though this is unlikely to be an important

$\Delta\rho$ (g/cm^3)	Gravity current head speed (g.c.) and 1st trailing internal wave phase speed (i.w.) (cm/s)							
	run 1		run 2		run 3		run 4	
	g.c.	i.w.	g.c.	i.w.	g.c.	i.w.	g.c.	i.w.
0.005	3.2	3.4	3.1	2.4	3.1	3.1	2.9	3.2
0.01	4.7	-	4.6	5.1	4.0	6.1	3.7	3.8
0.02	5.3	6.0	5.0	-	4.9	5.2	4.6	6.4
0.04	7.5	9.3	7.9	7.9	7.5	9.2	6.7	-

2h = 2 cm

Table 3.5: Speeds (± 1 cm/s) of the gravity current head (g.c.) and first trailing internal wave (i.w.) in four runs for an initial setup with $2h_i = 2$ cm. The '-' indicates no data recorded.

contributor since the vertical guide minimizes wave excitation.

On the fourth run of a series of experiments starting with $2h_i = 2$ cm, we observe a single double-humped wave, appearing in front of the gravity current head close to the end of the tank. The double-humped wave is actually made up of two waves, one of elevation propagating along the upper interface and one of depression propagating along the lower interface. We determined this disturbance to be two solitary waves propagating together in phase by observing that the potassium permanganate crystals dropped into the tank, which created roughly vertical tracks of dye, were displaced by the wave a finite distance roughly equal to the extent of the wave. This characteristic of solitary waves was noted by Russell (1844) upon observing (in the laboratory) the resulting net displacement of material particles suspended in a water channel as a solitary wave propagated along the water's surface.

Once the motions in the tank settle after an intrusion, the volume of the fluid that was behind the lock is distributed evenly along the middle layer of the three-layer fluid, thus thickening the interfacial layer by an amount equal to the volume behind

the lock:

$$\begin{aligned}
&\text{additional interfacial layer thickness} \\
&\quad = \frac{\text{volume of fluid to be distributed upon lock-release}}{\text{length of tank} \times \text{width of tank}} \\
&\quad = \frac{16 \text{ cm} \times 10 \text{ cm} \times 17.5 \text{ cm}}{197 \text{ cm} \times 17.5 \text{ cm}} \\
&\quad \approx 0.8 \text{ cm.}
\end{aligned}$$

Thus, in principle, on the fourth run of an experiment with $2h_i = 2$ cm, the gravity current propagates through an interfacial layer which is approximately 4.4 cm deep. For a larger interfacial layer thickness, we observed larger amplitude waves, extracting more momentum from the gravity current head, which stops propagating at a distance closer to the lock. Some of the excess momentum not lost to the trapped internal waves will manifest itself in the form of a solitary wave. It would then be reasonable to expect that the solitary wave appears sooner in the fourth run of an experiment with $2h_i = 2$ cm than it does for an experiment with $2h_i = 4$ cm. However, figure 3.12 indicates that this is not the case. In an experiment with $2h_i = 2$ cm, the repeated runs cause sufficient mixing so that the thickness over which the density varies is of the same order of magnitude as the initial middle layer thickness. That is, there is no longer a distinct 'step' profile as in the initial setup. For this new profile, the excess momentum lost from the gravity current head may not manifest itself immediately in the form of a solitary wave, rather, it may generate other unsteady semiperiodic waves (Davis & Acrivos, 1967). Thus the conditions under which the solitary wave appears in this altered system (with a new density profile created by mixing) are no longer described by the three-layer fluid theory which assumes three discrete layers. Instead, the motions in the tank may be better described by a theory for a two-layer system in which the two ambient layers are allowed to diffuse over time.

For a more direct comparison of the interfacial layer thickness in a three-layer fluid to the distance at which the solitary wave appears, we only consider the experiments in which the solitary wave appears on the first lock-release, before any mixing occurs

$\Delta\rho$ (g/cm^3)	Distance from lock at which the solitary wave separates from the gravity current head (cm)		
	$2h_i$ = 2 cm (4th run)	$2h_i$ = 3 cm	$2h_i$ = 4 cm
0.0025	95	110	80
0.005	112		95
0.01	125	90	97
0.02	150	140	97
0.03	175	180	110
0.04	180		112
0.05	does not appear		120

Table 3.6: Horizontal distance (± 2 cm) from the lock at which the solitary wave separates from the gravity current head. For $\Delta\rho = 0.05$, the solitary wave does not appear before the gravity current head reaches the end of the tank and is reflected.

at the interfaces in the ambient fluid. Estimates of the horizontal distance (± 2 cm) at which the solitary wave separates from the gravity current head (which in turn stops propagating) are shown in table 3.6. Since the distance along the tank at which the solitary wave appears lies outside the window in most cases, we make a rough estimate of this distance by marking on the tank wall the point at which the gravity current head stops and measuring the distance from the lock to this mark.

For a fixed $\Delta\rho$, the solitary wave appears at a further distance d along in the tank when $2h_i = 3$ cm than it does when $2h_i = 4$ cm, since the amplitudes of the trapped internal waves are smaller when $2h_i = 3$ cm than they are when $2h_i = 4$ cm. (This inverse relationship between d and the internal wave amplitude was predicted by (2.69). The increase in h causing a decrease in d is also predicted by the same equation.) It is also clear from figure 3.12 that for a given interfacial layer thickness the solitary wave appears further along in the tank for a higher $\Delta\rho$.

It is evident from table 3.7 that the momentum of the solitary wave M_{SW} is

$2h_1 = 4$ cm

$\Delta\rho$ (g/cm^3)	Components of Momentum Balance (10^2 g·cm/s)			error = $\left\| \frac{M_I - (M_{IW} + M_{SW})}{M_I} \right\|$
	M_I	M_{IW}	M_{SW}	
0.0025	3	1	1	0.3
0.005	4	2	1	0.3
0.01	6	5	2	0.2
0.02	8	6	3	0.1
0.03	10	7	3	0
0.04	12	9	4	0.1
0.05	13	10	4	0.1

$2h_1 = 3$ cm

$\Delta\rho$ (g/cm^3)	Components of Momentum Balance (10^2 g·cm/s)			error = $\left\| \frac{M_I - (M_{IW} + M_{SW})}{M_I} \right\|$
	M_I	M_{IW}	M_{SW}	
0.0025	3	2	1	0
0.01	6	3	2	0.2
0.02	9	5	2	0.2
0.03	11	7	3	0.1

Table 3.7: Estimates of components of momentum for several experiments. The components are given by (2.66) for initial momentum M_I, (2.67) for internal wave momentum M_{IW} and (2.68) for solitary wave momentum M_{SW}. Upper bounds on the error are estimated to be $\pm 5\%$ for M_I, $\pm 20\%$ for M_{SW} and $\pm 25\%$ for M_{IW}.

always approximately one third of the initial momentum M_I, that is, a solitary wave is generated after the gravity current has transferred approximately two thirds of its momentum to the internal waves. Since an increase in $\Delta\rho$ results in a greater initial momentum of the current, a greater amount of momentum must be transferred to the internal waves before a solitary wave (which requires a fixed percentage of the initial momentum) will be excited. Consequently, the current must propagate further along the tank before momentum is completely lost to the trapped internal waves and the solitary wave. We suggest that a fixed percentage of the initial momentum is extracted by the solitary wave because it has a fixed size and speed which depends

L (cm)	d (cm)
20	132
30	100
40	90

$\Delta\rho = 0.02$ g/cm^3

Table 3.8: Distance d (± 2 cm) at which the solitary wave is excited for three different lock-lengths L.

on the initial setup of the experiment.

According to (2.66), for a fixed $\Delta\rho$, the current has a greater initial momentum for a smaller interfacial layer thickness h. Thus more momentum needs to be extracted from the gravity current before $\frac{1}{3}M_I$ (an empirical observation) remains, at which stage the solitary wave is excited. The smaller amplitude waves associated with smaller h cause momentum to be extracted from the current at a slower rate. This allows the current to propagate further along the tank before the solitary wave is excited.

In the preliminary series of experiments in which a three-layer system was created by an intrusion into a two-layer system, the effect of changing the lock-length L was observed. For a fixed value of $\Delta\rho$, the distance d at which the solitary wave was excited was measured on the third run of three different experiments with $L = 20$, 30 and 40 cm as shown in table 3.8. As expected, larger L corresponded to a larger increase in interfacial layer thickness, which in turn corresponds to smaller d. This was predicted by (2.69). (It is also interesting to note that for larger L, a longer gravity current head was observed, which was estimated to be roughly equal to the length of the lock.)

Like the gravity current head speed, the solitary wave speed also increases as $\Delta\rho$ increases as shown in figure 3.13. We find that the estimated average maximum height a of the solitary wave is 2.4 ± 1 cm for experiments with $2h_i = 3$ cm and 2.1 ± 1 cm for experiments with $2h_i = 4$ cm. Again, since the solitary wave appears outside of

the window in most cases, an intensity enhanced digitized image could not be used to determine the maximum wave amplitude. Instead, we resort to rough estimates obtained by marking the wave height on the tank wall and measuring the distance from $z = 0$ to the mark. According to Benjamin's (1967) theoretical solitary wave speed (2.55), $c_{B67} = \sqrt{g'h(1 + \frac{3}{4}\frac{a}{h})}$, a larger interfacial layer thickness corresponds to a greater wave speed for a fixed density difference. (Note the dashed line above the solid line in figure 3.13.) The data given in figure 3.13 indicate the same trend. We also see that the observed solitary wave speeds for a particular interfacial layer thickness are slower than the corresponding theoretical values, due to viscous dissipation extracting energy from the main motion. This was neglected in the theory. In fact, the observed solitary wave speeds are closer to the linear wave speed given by $c_0 = \sqrt{g'h}$ for density differences between $\Delta\rho = 0.0025$ and 0.05 g/cm^3.

Finally, we examine the applicability of the idealized momentum balance (2.62) given in the previous chapter. The initial momentum M_I, the momentum carried by the internal waves M_{IW} and the momentum of the solitary wave M_{SW} (given by (2.66), (2.67) and (2.68) respectively) were estimated using typical numbers from the experiments. The results, which show agreement with the theoretical balance within a reasonable margin of error, are shown in table 3.7. The large source of error for the computed internal wave momentum and the solitary wave momentum lies in the sensitivity to the data (*e.g.*, for the internal wave momentum, there is a strong dependence on the accuracy of the wave amplitude). In addition, the error in the balance also suggests that some of the assumptions made in the theory (*e.g.*, neglecting losses due to turbulent mixing when deriving an initial velocity for the intrusion (2.65)) may not reflect the behaviour in the experiments. As previously mentioned, the table strongly suggests that in order for a solitary wave to be excited, the fraction of the internal wave momentum that is transferred to the solitary wave is fixed. In our experiments, $M_{SW} \approx \frac{1}{3}M_I$. Since the amplitude a of the solitary wave is roughly the same for each experiment for a fixed interfacial layer thickness h, the

momentum of the solitary wave must depend on $\Delta\rho$. In fact, M_{SW} increases as the square root of the density difference. For example, if $\Delta\rho$ is increased by a factor of 4, then M_{SW} increases by a factor of 2. This general trend can also be seen in table 3.7.

3.3 Future Improvements on Data Collection

As mentioned above, data for the density profiles at various stages throughout an experiment was obtained by discrete conductivity probe measurements at different depths in the three-layer fluid. The large discrepancy between the actual density of the middle and upper layers and the measured density at the $z = 0$ and $z = -8$ cm could be due to small scale wave motions caused by any jarring motion when moving the probe down, fluctuations in the electrical power from the external power source feeding the probe, or inaccurate calibration solutions. A smoother and more accurate density profile would be obtained with the use of a traverse, producing an effectively continuous profile. A continuous traverse may also sufficiently reduce the wave motions in the tank to obtain more accurate density measurements. Multiple traverses at different positions along the length of the tank would allow for an average density profile to be considered.

For all of the data collected using DigImage, the video camera was focused on a small section of the tank. However, some of the measurements needed to be taken outside the 20 cm window, such as the distance at which the solitary wave separates from the gravity current head, the speed of the solitary wave when $2h_i = 2$ cm and its amplitude. Focusing on a larger segment of the tank would sacrifice the accuracy of the measurements taken from the digitized images. A second camera would allow for measurements in more than one location along the length of the tank, without sacrificing accuracy.

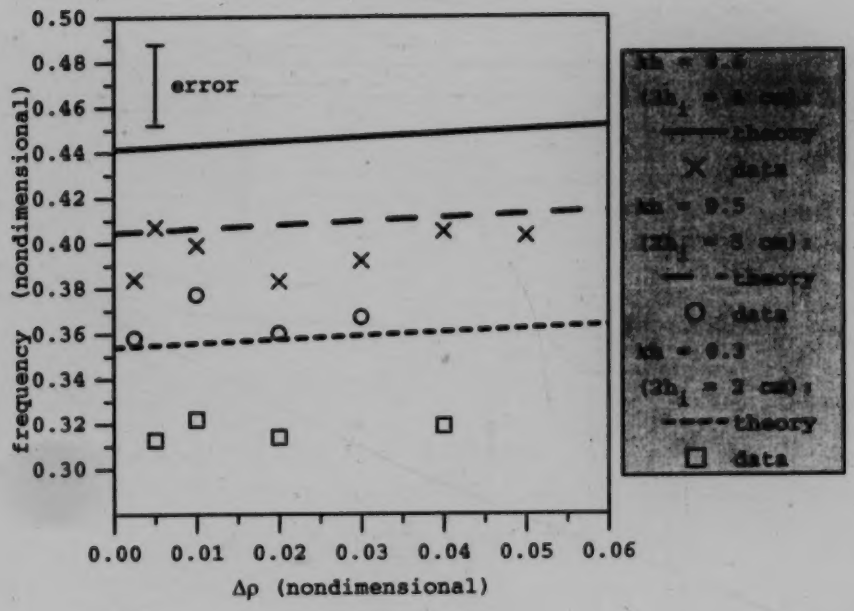

Figure 3.8: Frequency as a function of $\Delta\rho$ for three different values of kh, and data from experiments with similar values for kh.

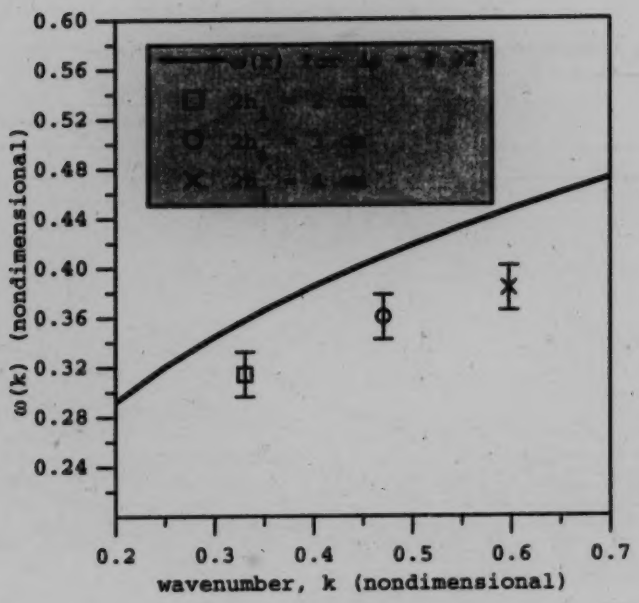

Figure 3.9: Dispersion relation for $\Delta\rho$ (nondimensional) = 0.02 as a function of kh, and data from experiments with similar values for kh.

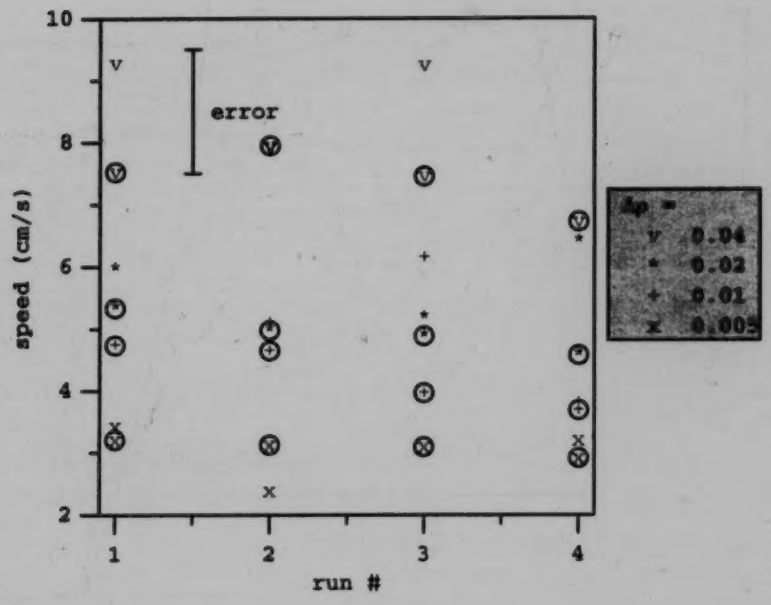

Figure 3.10: Gravity current head speeds (indicated with ◯) and trailing internal wave speeds (no ◯) for experiments with different $\Delta\rho$. The initial setup has $2h_i = 2$ cm.

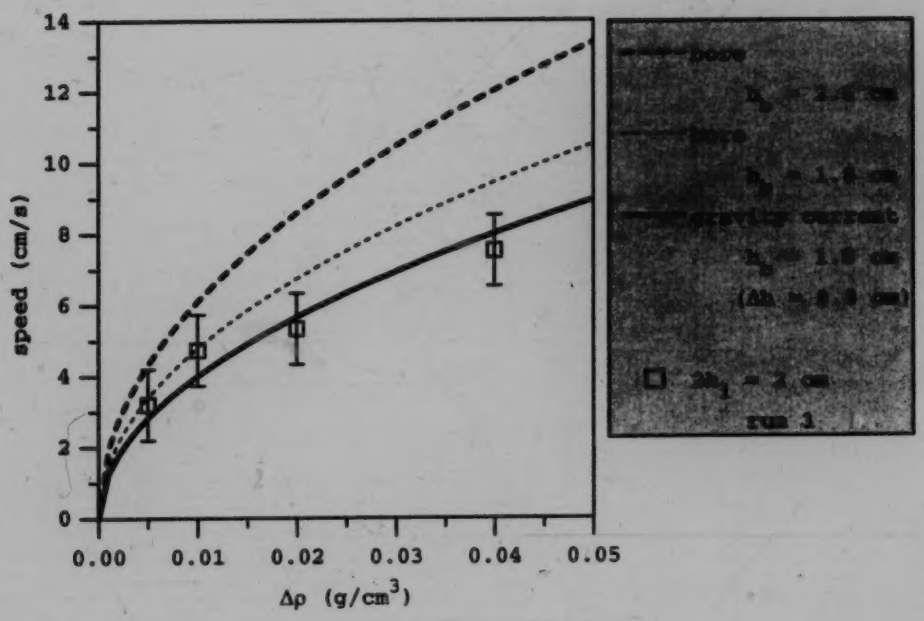

Figure 3.11: Gravity current speed given by (2.36) for $\Delta h = 0.8$ cm, bore speed given by (2.49) for $h_b = 1.8$ (mean height, measured from $z = 0$, of the tail behind the current head from each experiment) and $h_b = 2.6$ cm (mean height, measured from $z = 0$, of the gravity current head from each experiment), along with observed data for gravity current speeds during the initial intrusion when $2h_i = 2$ cm.

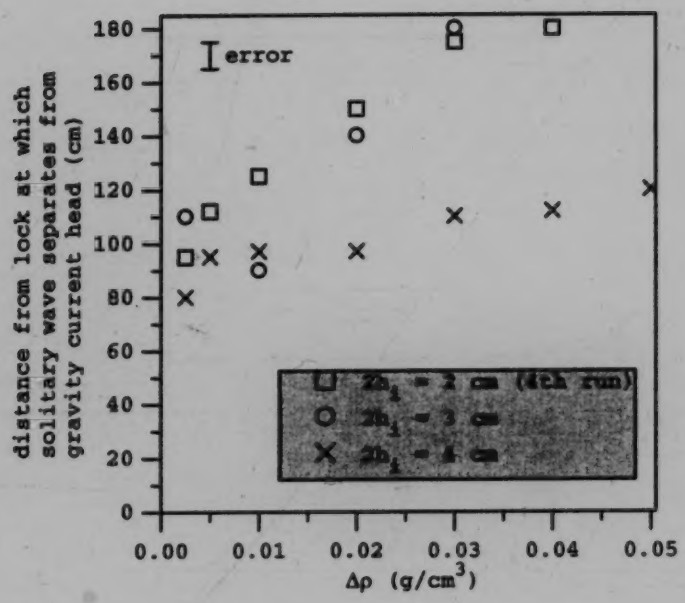

Figure 3.12: Horizontal distance (±2 cm) from the lock at which the solitary wave separates from the gravity current head for various $\Delta\rho$ when $2h_i = 2$, 3 and 4 cm.

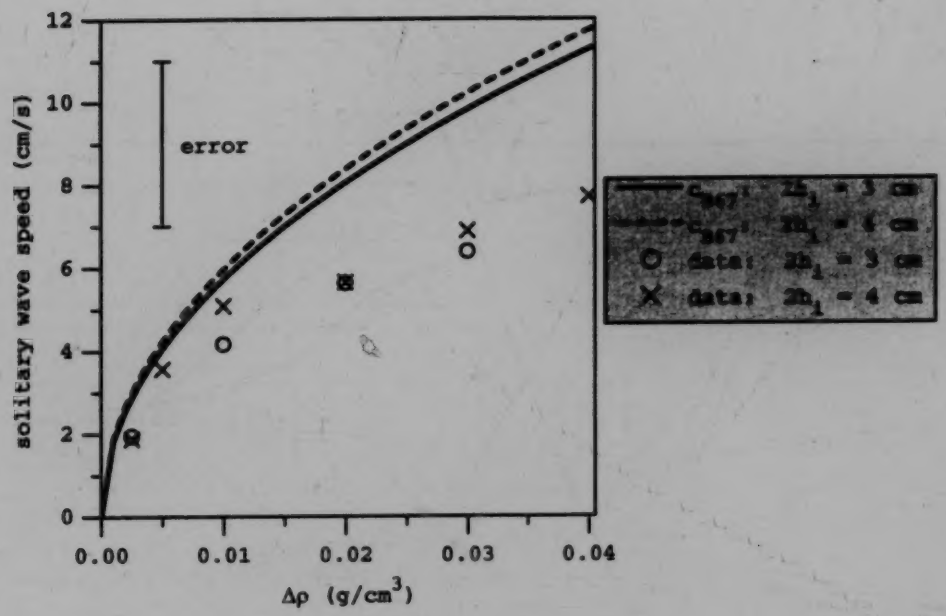

Figure 3.13: Solitary wave speeds as a function of $\Delta\rho$ given by (2.55) for $2h_i = 3$ cm (estimated average maximum height $a = 2.4 \pm 1$ cm) and $2h_i = 4$ cm (estimated average maximum height $a = 2.1 \pm 1$ cm), and observed data (± 2 cm/s) from experiments with corresponding $2h$.

Chapter 4

Conclusions

In an effort to better understand atmospheric and oceanic phenomena involving intrusions in a density-stratified fluid, we conducted a theoretical and experimental investigation of a three-layer fluid.

The experiments in the present study showed no significant interaction with the walls of the fluid tank. Thus, assuming free-slip at the walls of the tank, and assuming the effects of viscosity and external forces, aside from gravity, to be negligible, an attempt was made to model the experimental observations by theoretical analysis. With a reasonable margin of error, it was shown that the theory developed for a three-layer fluid was applicable to the experimental observations.

For an irrotational, incompressible, inviscid three-layer fluid, we derived two dispersion relations (and thus, two phase speeds), one corresponding to a sinuous mode and one corresponding to a varicose mode. A limiting case of the sinuous mode was shown to agree with the dispersion relation and phase speed of internal waves in a two-layer fluid. By using numerical code based on solving the Taylor-Goldstein equation, we determined that the three-layer theoretical dispersion relations based on a discrete stratification adequately represented the experimental case in which the density varied continuously over a very thin region between two adjacent layers of fluid.

We also provided a derivation for the speed of propagation of a gravity current intruding through the middle layer of a three-layer fluid. In the Boussinesq limit, we presumed that it was sufficient to determine the propagation speed of a gravity current of density ρ_1 propagating through the upper layer of a two-layer fluid with densities ρ_1 and $\rho_2 > \rho_1$.

Rather than deriving the speed of the double-humped solitary wave propagating along the upper and lower interfaces of a three-layer fluid, it was suggested that for an appropriate first approximation, the solitary wave speed in a two-layer fluid previously derived by Benjamin (1967) could be used in the case of a Boussinesq fluid. Since the density difference between the adjacent layers of the three-layer fluid was small, we assumed that the elevated and depressed solitary waves comprising the double-humped solitary wave propagated at the same speed (as suggested by experimental observations).

These theoretical results were then combined in a momentum balance, in which we assumed that the total momentum of the gravity current was lost to the generation of trapped internal waves and a double-humped solitary wave.

The data collected from the experiments was compared to the theoretical results to determine the applicability of the theory to observations. In addition to concluding that the present three-layer fluid theory sufficiently describes the three-layer fluid experiments, we may summarize the observations as follows.

Defining nondimensional parameters

$$S = \sqrt{\frac{h}{H}}$$

and

$$G = \frac{\Delta\rho}{\rho_0},$$

we observe for $S \ll 1$ a gravity current head with very small amplitude trapped internal waves attenuating rapidly. For $S = \frac{1}{3}$, we observe a gravity current head with a tail, but no solitary wave appears over the extent of the tank. When S is roughly

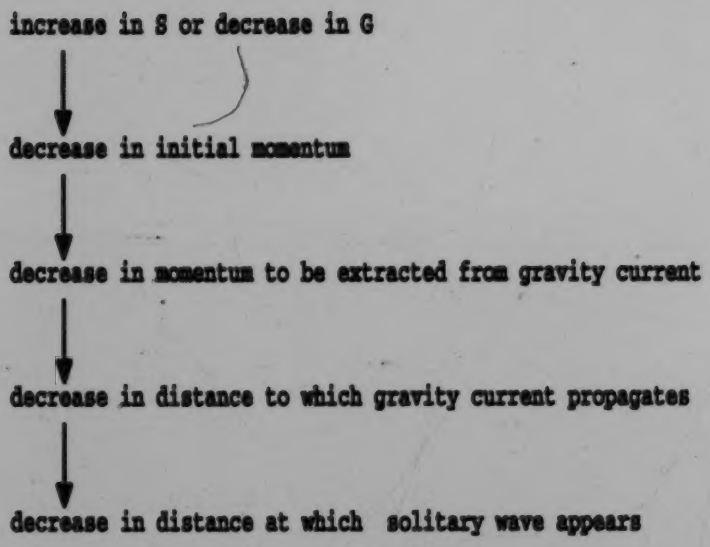
increase in S or decrease in G
decrease in initial momentum
decrease in momentum to be extracted from gravity current
decrease in distance to which gravity current propagates
decrease in distance at which solitary wave appears

Figure 4.1: Chain of effects.

greater than 0.4, we observe a gravity current head with a tail and the appearance of a solitary wave. For $G = 0.0025$ and $S = \frac{1}{3}$, the measured amplitude of the waves starts at roughly 0.2 cm with exponential decay and the gravity current head propagates at roughly 2 cm/sec. As G increases, the speed of the gravity current head also increases. We also observe less significant amplitude attenuation as S increases.

With a lock length of 10 cm and S close to $\frac{1}{2}$ we find that for $G = 0.0025$, the solitary wave appears at 8 lock-lengths from the gate. When G is increased to 0.05 (20 times greater) the measured amplitude of the waves is 2 times larger with no noticable decay and the speed of propagation of the gravity current head is 4 times faster. In addition, at a higher density difference, the initial momentum M_I is greater, and therefore more momentum must be extracted from the gravity current by the trapped internal waves so that a solitary wave may be excited with a momentum approximately equal to $\frac{1}{3}M_I$. Thus the solitary wave appears further along in the tank at 12 lock-lengths. Figure 4.1 shows the effects of changing S or G.

We propose that a resonant coupling of the gravity current head with the trapped

internal waves is the underlying reason for the transition from gravity current propagation to internal gravity waves and solitary wave propagation. That is, the gravity current head and trapped internal waves together excite a solitary wave.

Motivated by the Morning Glory phenomenon, this study of a three-layer incompressible, irrotational, inviscid fluid neglecting background shear is clearly a significant simplification of the phenomenon it attempts to model, however, it does present a starting point.

In the experimental and theoretical investigation conducted, the middle layer density was restricted to be equal to the mean of the upper and lower layer densities, and the depths of the upper and lower layers were the same. In future study of a three-layer fluid one may wish to relax this restriction, such that $\rho_1 - \rho_0 \neq \rho_2 - \rho_1$, to expand the theory and experimental study. We may then presume that the two solitary waves (making up the double-humped solitary wave) initially generated by the gravity current head may not continue to travel together in phase. In this case, symmetry arguments (assumed in the present theory for a Boussinesq fluid) may not adequately represent the experiments.

Secondly, the assumptions of an incompressible, irrotational, inviscid fluid could be discarded, thus providing a set of nonlinear governing equations, which may be solved numerically. Thirdly, an extension of this study to three dimensions would be valuable, particularly to investigate the effects of the earth's rotation on large-scale flows. Fourthly and finally, the study could be further extended to include the effects of background velocity gradient on a continuously stratified system which would more closely resemble the stratification and shear present in various atmospheric and oceanic phenomena, such as the beautiful Morning Glory of Australia.

Bibliography

[1] Abdullah, A. J. 1949 Cyclogenesis by a purely mechanical process. *J. Meteor.* **6,** 86-97.

[2] Abdullah, A. J. 1955 The atmospheric solitary wave. *Bull. Amer. Met. Soc.* **36,** 515-518.

[3] Abdullah, A. J. 1956 A note on the atmospheric solitary wave. *J. Meteor.* **13,** 381-387.

[4] Amick, C. J. & Turner, R. E. L. 1986 Internal solitary waves in a two-fluid system. *Trans. Am. Math. Soc.* **298,** 431-484.

[5] Benjamin, T. B. 1966 Internal waves of finite amplitude and permanent form. *J. Fluid Mech.* **25,** 241-270.

[6] Benjamin, T. B. 1967 Internal waves of permanent form in fluids of great depth. *J. Fluid Mech.* **29,** 559-592.

[7] Benjamin, T. B. 1968 Gravity currents and related phenomenon. *J. Fluid Mech.* **31,** 209-248.

[8] Benney, C. J. 1966 Long nonlinear waves in fluid flows. *J. Math. Phys.* **45,** 52-63.

[9] Boussinesq, J. 1871 Théorie de l'intumescence liquide appelée onde solitaire ou de translation se propageant dans un canal rectangulaire. *Inst. France Acad. Sci. Comptes Rendus* **72,** 755-759.

[10] Britter, R. E. & Simpson, J. E. 1981 A note on the structure of the head of an intrusive gravity current. *J. Fluid Mech.* **112,** 459-466.

[11] Bullough, R. K. 1987 "The Wave" "Par Excellence", the solitary progressive great wave of equilibrium of the fluid: an early history of the solitary wave. In *Solitons: Introduction and Applications* (ed. M. Lakshmanan), 7-42. Springer-Verlag.

[12] Christie, D. R. 1989 Long nonlinear waves in the lower atmosphere. *J. Atmos. Sci.* **46,** 1462-1491.

[13] Christie, D. R. 1992 The morning glory of the Gulf of Carpentaria: a paradigm for non-linear waves in the lower atmosphere. *Aust. Met. Mag.* **41,** 21-60.

[14] Christie, D. R., Muirhead, K. J. & Clarke, R. H. 1981 Solitary waves in the lower atmosphere. *Nature* **293,** 46-49.

[15] Christie, D. R., Muirhead, K. J. & Hales, A. L. 1978 On solitary waves in the atmosphere. *J. Atmos. Sci.* **35,** 805-825.

[16] Christie, D. R., Muirhead, K. J. & Hales, A. L. 1979 Intrusive density flows in the lower troposphere: a source of atmospheric solitons. *J. Geophys. Res.* **84,** 4959-4970.

[17] Clarke, J. C. 1998 Picture of the Month: An atmospheric undular bore along the Texas coast. *Mon. Weather Rev.* **126,** 1098-1100.

[18] Clarke, R. H. 1972 The morning glory: an atmospheric hydraulic jump. *J. Appl. Meteorol.* **11,** 304-311.

[19] Clarke, R. H. 1983 Fair weather nocturnal inland wind surges and bores, Part II. Internal atmospheric bores in northern Australia. *Aust. Met. Mag.* **31,** 147-160. (Corrigenda, *Aust. Met. Mag.* **32,** 53.)

[20] Clarke, R. H., Smith, R. K. & Reid, D. G. 1981 The morning glory of the Gulf of Carpentaria: an atmospheric undular bore. *Mon. Weather Rev.* **109,** 1726-1750.

[21] Davis, R. E. & Acrivos, A. 1967 Solitary internal waves in deep water. *J. Fluid Mech.* **29,** 593-607.

[22] Drazin, P. G. & Johnson, R. S. 1989 *Solitons: an introduction.* Cambridge University Press.

[23] Drazin, P. G. & Reid, W. H. 1981 *Hydrodynamic Stability.* Cambridge University Press.

[24] Holyer, J. Y. & Huppert, H. E. 1980 Gravity currents entering a two-layer fluid. *J. Fluid Mech.* **100,** 739-767.

[25] Hurdis, D. A., & Pao, H.-P. 1975 Experimental observations of internal solitary waves in a stratified fluid. *Phys. Fluids* **18,** 385-386.

[26] Joseph, R. I. 1977 Solitary waves in a finite depth fluid. *J. Phys. A: Math. Gen.* **10,** L225-L227.

[27] Keulegan, G. H. 1953 Characteristics of internal solitary waves. *J. Res. Nat. Bur. Stand.* **51,** 133-140.

[28] Klemp, J. B., Rotunno, R. & Skamarock, W. C. 1994 On the dynamics of gravity currents in a channel. *J. Fluid Mech.* **269,** 169-198.

[29] Klemp, J. B., Rotunno, R. & Skamarock, W. C. 1997 On the propagation of internal bores. *J. Fluid Mech.* **331,** 81-106.

[30] Koop, C. G. & Butler G. 1981 An investigation of internal solitary waves in a two-fluid system. *J. Fluid Mech.* **112,** 225-251.

[31] Korteweg, D. J. & de Vries, G. 1895 On the change of form of long waves advancing in a rectangular canal, and on a new type of long stationary waves. *Phil. Mag.* (5) **39,** 422-443.

[32] Kundu, P. K. 1990 *Fluid Mechanics.* Academic Press.

[33] Linden, P. F. & Simpson, J. E. 1985 Microbursts: a hazard for aircraft. *Nature* **317,** 601-602.

[34] Long, R. R. 1956 Solitary waves in one- and two-fluid systems. *Tellus* **8,** 460-471.

[35] Manasseh, R., Ching, C.-Y. & Fernando, H. J. S. 1998 The transition from density-driven to wave-dominated isolated flows. *J. Fluid Mech.* **361,** 253-274.

[36] Maxworthy, T. 1980 On the formation of nonlinear internal waves from the gravitational collapse of mixed fluid regions in two and three dimensions. *J. Fluid Mech.* **96,** 47-64.

[37] Menhofer, A., Smith, R. K., Reeder, M. J. & Christie, D. R. 1997 'Morning-glory' disturbances and the environment in which they propagate. *J. Atmos. Sci.* **54,** 1712-1725.

[38] Michallet, H. & Barthélemy, E. 1998 Experimental study of interfacial solitary waves. *J. Fluid Mech.* **366,** 159-177.

[39] Miles, J. W. 1979 On internal solitary waves. *Tellus* **31,** 456-462.

[40] Noh, Y., Fernando, H. J. S. & Ching, C.-Y. 1992 Flows induced by the impingement of a two-dimensional thermal on a density interface. *J. Phys. Ocean.* **22,** 1207-1220.

[41] Noonan, J. A. & Smith, R. K. 1985 Linear and weakly nonlinear internal wave theories applied to 'morning glory' waves. *Geophys. Astrophys. Fluid Dyn.* **33,** 123-143.

[42] Ono, H. 1975 Algebraic solitary waves in stratified fluids. *J. Phys. Soc. Japan* **39,** 1082-1091.

[43] Ostrovsky, L. A. & Stepanyants, Y. A. 1989 Do internal solitons exist in the ocean? *Rev. Geophys.* **27,** 293-310.

[44] Pedlosky, J. 1979 *Geophysical Fluid Dynamics,* second edition. Springer-Verlag.

[45] Peters, A. S. & Stoker, J. J. 1960 Solitary waves in liquids having non-constant density. *Comm. Pure Appl. Math.* **13,** 115-164.

[46] Pullin, D. I. & Grimshaw, R. H. J. 1988 Finite-amplitude solitary waves at the interface between two homogeneous fluids. *Phys. Fluids* **31,** 3550-3559.

[47] Rayleigh, Lord 1876 On waves. *Phil. Mag.* (5) **1,** 257-279.

[48] Rottman, J. W. & Simpson, J. E. 1989 The formation of internal bores in the atmosphere: a laboratory model. *Q. J. R. Met. Soc.* **115,** 941-963.

[49] Russell, J. S. 1844 Report on Waves. *Brit. Assoc. Rep.* No. 311.

[50] Simpson, J. E. 1997 *Gravity Currents in the Environment and the Laboratory,* second edition. Cambridge University Press.

[51] Simpson, J. E. & Britter, R. E. 1979 The dynamics of the head of a gravity current advancing over a horizontal surface. *J. Fluid Mech.* **94,** 477-495.

[52] Simpson, J. E. Mansfeild, D. A. & Milford, J. R. 1977 Inland penetration of seabreeze fronts. *Q. J. R. Met. Soc.* **103,** 47-76.

[53] Smith, R. K., Coughlan, M. J. & Lopez, J.-L. 1986 Southerly nocturnal wind surges and bores in northeastern Australia. *Mon. Weather Rev.* **114,** 1501-1518.

[54] Smith, R. K., Crook, N. & Roff, G. 1982 The morning glory: an extraordinary undular bore. *Q. J. R. Met. Soc.* **108,** 937-956.

[55] Smith, R. K. & Ridely, R. N. 1990 Subtropical continental cold fronts. *Aust. Met. Mag.* **38,** 191-200.

[56] Stamp, A. P. & Jacka, M. 1995 Deep-water internal solitary waves. *J. Fluid Mech.* **305,** 347-371.

[57] Sutherland, B. R. & Peltier, W. R. 1992 The stability of stratified jets. *Geophys. Astrophys. Fluid Dyn.* **66,** 101-131.

[58] Thorpe, S. A. 1971 Experiments on the instability of stratified shear flows: miscible fluids. *J. Fluid Mech.* **46,** 299-319.

[59] Wood, I. R. & Simpson, J. E. 1984 Jumps in layered miscible fluids. *J. Fluid Mech.* **140**, 329-342.

[60] Yih, C.-S. & Guha, C. R. 1955 Hydraulic jump in a fluid system of two layers. *Tellus* **7**, 359-366.